







Global Biogeochemical Cycles®



RESEARCH ARTICLE

10.1029/2024GB008315

Trends in Sea-Air CO₂ Fluxes and Sensitivities to Atmospheric Forcing Using an Extremely Randomized Trees Machine Learning Approach

Rik Wanninkhof¹ , Joaquin Triñanes^{1,2,3} , Denis Pierrot¹ , David R. Munro^{4,5} ,
Colm Sweeney⁴ , and Amanda R. Fay⁶ 

Key Points:

- An extremely randomized trees machine learning approach yields a global CO₂ flux of $-1.70 \text{ PgC yr}^{-1}$ with a trend of $-0.89 \text{ PgC yr}^{-1} \text{ decade}^{-1}$
- The trend changes to $-0.51 \text{ PgC yr}^{-1} \text{ decade}^{-1}$ when the target is changed from CO₂ fugacity in water to sea-air CO₂ fugacity difference
- Different atmospheric CO₂ forcing has a large impact on the magnitude and trends of global and regional sea-air fluxes

¹Atlantic Oceanographic and Meteorological Laboratory, National Oceanic and Atmospheric Administration, Miami, FL, USA, ²Rosenstiel School of Marine, Atmospheric and Earth Science, Cooperative Institute for Marine and Atmospheric Studies, University of Miami, Miami, FL, USA, ³Department of Electronics and Computer Science, Universidade de Santiago de Compostela, Santiago, Spain, ⁴Global Monitoring Laboratory, National Oceanic and Atmospheric Administration, Boulder, CO, USA, ⁵Cooperative Institute for Research in Environmental Sciences (CIRES), University of Colorado, Boulder, CO, USA, ⁶Columbia University and Lamont-Doherty Earth Observatory, Palisades, NY, USA

Supporting Information:

Supporting Information may be found in the online version of this article.

Correspondence to:

R. Wanninkhof,
rik.wanninkhof@noaa.gov

Citation:

Wanninkhof, R., Triñanes, J., Pierrot, D., Munro, D. R., Sweeney, C., & Fay, A. R. (2025). Trends in sea-air CO₂ fluxes and sensitivities to atmospheric forcing using an extremely randomized trees machine learning approach. *Global Biogeochemical Cycles*, 39, e2024GB008315. <https://doi.org/10.1029/2024GB008315>

Received 26 JUL 2024

Accepted 26 DEC 2024

Author Contributions:

Conceptualization: Rik Wanninkhof, Joaquin Triñanes, Colm Sweeney
Data curation: Amanda R. Fay
Formal analysis: Rik Wanninkhof, David R. Munro, Colm Sweeney, Amanda R. Fay
Investigation: Colm Sweeney
Methodology: Rik Wanninkhof, Joaquin Triñanes, Denis Pierrot, David R. Munro, Colm Sweeney, Amanda R. Fay
Software: Joaquin Triñanes

Published 2025. This article is a U.S. Government work and is in the public domain in the USA. *Global Biogeochemical Cycles* published by Wiley Periodicals LLC on behalf of American Geophysical Union.

This is an open access article under the terms of the [Creative Commons Attribution License](https://creativecommons.org/licenses/by/4.0/), which permits use, distribution and reproduction in any medium, provided the original work is properly cited.

Abstract Monthly global sea-air CO₂ flux maps are created on a 1° by 1° grid from surface water fugacity of CO₂ (fCO_{2w}) observations using an extremely randomized trees (ET) machine learning technique (AOML-ET) over the period 1998–2020. Global patterns and magnitudes of fCO_{2w} from AOML-ET are consistent with other machine learning methods and with the updated climatology of Takahashi et al. (2009, <https://doi.org/10.1016/j.dsr2.2008.12.009>). However, the magnitude and trends of sea-air CO₂ fluxes are sensitive to the treatment of atmospheric forcing. In the default configuration of AOML-ET, the average global sea-air CO₂ flux is $-1.70 \text{ PgC yr}^{-1}$ with a negative trend of $-0.89 \pm 0.19 \text{ PgC yr}^{-1} \text{ decade}^{-1}$. The large negative trend is driven by a small uptake at the beginning of the record. This leads to increasing sea-air fCO₂ gradients over time, particularly at high latitudes. However, changing the target variable in AOML-ET from fCO_{2w} to sea-air CO₂ fugacity difference, ΔfCO_2 , results in a lower negative trend of $-0.51 \text{ PgC yr}^{-1} \text{ decade}^{-1}$, though the average flux remains similar at $-1.65 \text{ PgC yr}^{-1}$. This trend is close to the consensus trend of ocean uptake from machine learning and models in the Global Carbon Budget of $-0.46 \pm 0.11 \text{ PgC yr}^{-1} \text{ decade}^{-1}$ switching to a gas transfer parameterization with weaker wind speed dependence reduces uptake by 60% but does not affect the trend. Substituting a spatially resolved marine air CO₂ mole fraction product for the zonally invariant marine boundary layer CO₂ product yields greater influx by up to 20% in the industrialized continental outflow regions.

Plain Language Summary Machine learning approaches are increasingly applied to create global monthly surface ocean fugacity of carbon dioxide (fCO_{2w}) fields and are used in global carbon budget assessments. Here we use an extremely randomized tree machine learning approach (AOML-ET) to map fCO_{2w} and calculate monthly global sea-air CO₂ fluxes from 1998 to 2020. The patterns and magnitude of monthly mapped fCO_{2w} fields on a 1° by 1° grid are very similar to other machine learning methods and also to the canonical climatology of Takahashi et al. (2009, <https://doi.org/10.1016/j.dsr2.2008.12.009>). However, the global CO₂ uptake trend using AOML-ET in its default configuration is much larger, at $-0.89 \pm 0.19 \text{ PgC yr}^{-1} \text{ decade}^{-1}$, compared to $-0.46 \pm 0.11 \text{ PgC yr}^{-1} \text{ decade}^{-1}$ for the consensus value of the Global Carbon Budget from 1998 to 2020. We investigate the sensitivity to changing predictors and target variables, which shows that substituting predictors has little effect. However, by changing the target in the machine learning step of AOML-ET from fCO_{2w} to sea-air CO₂ fugacity difference, ΔfCO_2 , the trend changes to $-0.51 \text{ PgC yr}^{-1} \text{ decade}^{-1}$. Changing the atmospheric forcing using different marine CO₂ boundary layer products or gas exchange parameterizations has a large impact on sea-air CO₂ fluxes. A parameterization that meets the same global constraint as other functionalities but with a lower dependency on wind speed decreases ocean CO₂ uptake by up to 60% but does not impact the trend in uptake over the time period.

1. Introduction

Sea-air CO₂ fluxes are the primary conduit for the transfer and subsequent storage of anthropogenic CO₂ in the ocean. This leads to increased surface water CO₂ concentrations, which contribute to surface ocean acidification (Doney et al., 2020; Iida et al., 2021). Quantifying the fluxes is critical for the Global Stocktake, which reviews

Validation: Joaquin Triñanes, Denis Pierrot
Visualization: Joaquin Triñanes
Writing – original draft: Rik Wanninkhof, Joaquin Triñanes, Denis Pierrot, David R. Munro
Writing – review & editing: Rik Wanninkhof, Colm Sweeney, Amanda R. Fay

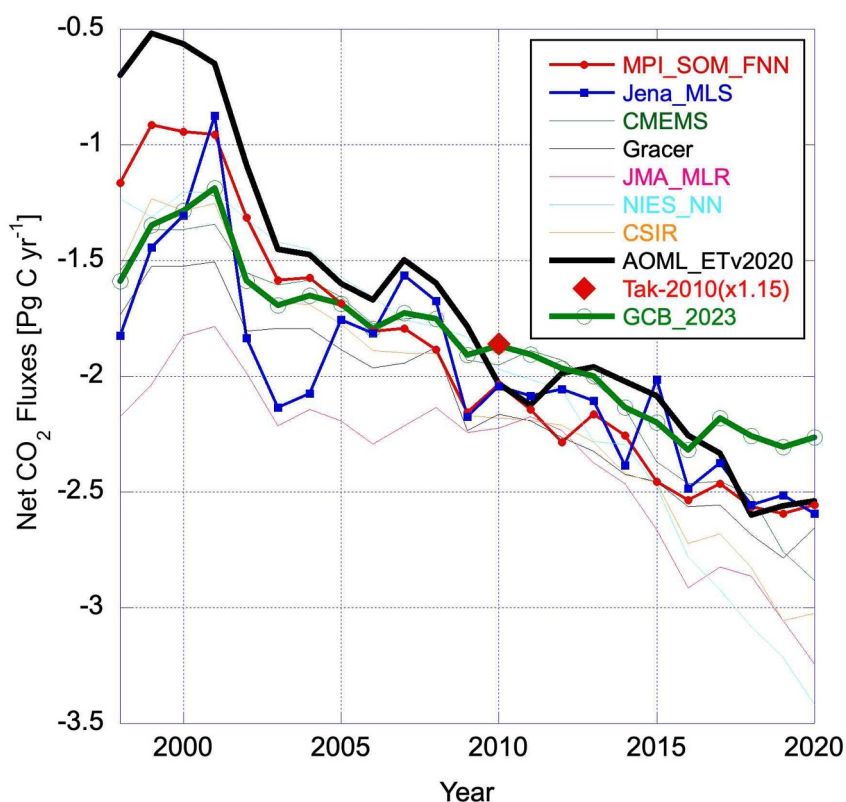


Figure 1. Global annual net sea-air CO₂ fluxes from 1998 to 2020 determined by a variety of ML and regression approaches. Data, other than AOML-ET and Tak-2010 (x1.15), where x1.15 indicates it is multiplied by 1.15 to normalize for area, are estimates of anthropogenic CO₂ uptake from <https://globalcarbonbudgetdata.org/latest-data.html> [Global_Carbon_Budget_2022v1.0.xlsx]. For these results, 0.65 PgC is added onto the anthropogenic CO₂ fluxes from the GCP to obtain the net sea-air CO₂ flux. For references to the methods, see the caption of Table 1.

progress toward the Paris Agreement goals every 5 years (Magnan et al., 2016). The fluxes can also be used to determine how the oceanic sink changes on seasonal to decadal timescales. Several assessments of the global ocean CO₂ sink are available. Annual updates on anthropogenic CO₂ uptake by the oceans are provided in the Global Carbon Budget (GCB) (Friedlingstein et al., 2023), while pentadal updates of both anthropogenic and net CO₂ uptake are available through the Regional Carbon Cycle Assessment and Processes (RECCAP). Both these assessments use a variety of approaches to determine the ocean carbon sink. The RECCAP2 analysis yields a sea-air CO₂ flux of -1.6 ± 0.2 PgC yr⁻¹ based on an ensemble of 11 observation-based machine learning (ML) and regression approaches for sea surface pCO₂ from 1985 to 2018 (de Vries et al., 2023). The GCB-2023 consensus value based on models and observations produces a value of -1.85 ± 0.32 PgC yr⁻¹ and a trend of -0.46 ± 0.11 PgC yr⁻¹ decade⁻¹ from 1998 to 2020, calculated from data in <https://globalcarbonbudgetdata.org/latest-data.html> [Global_Carbon_Budget_2022v1.0.xlsx]. The annual global ocean CO₂ uptake with time is shown in Figure 1 for eight of the approaches. There is overall concordance in global magnitude and variability across the different approaches, but they show a range of decadal trends and notable regional differences. The observation-based estimates used the same database of monthly gridded surface water fugacity (fCO_{2w}) values from SOCAT (Bakker et al., 2016), along with similar atmospheric forcing for CO₂ values in air and gas transfer velocities. This creates a skewed perspective of agreement between the different estimates of sea-air CO₂ fluxes, as only differences in the mapping of fCO_{2w} fields using machine learning or interpolation methods are considered.

Early synthesis efforts to determine global and regional CO₂ flux patterns focused on creating a fixed monthly climatology through extrapolation of surface partial pressure of CO₂ (pCO_{2w}) data (Fay et al., 2024; Takahashi et al., 1997, 2009). The climatology used much of the available pCO₂ data at the time, normalized to a specific year, and presented per month on a 4° by 5° grid. Interannual variability was estimated using this product by determining correlations between SST and pCO_{2w} at the grid scale (Lee et al., 1998; Park et al., 2010). Here, we

use the appropriate parameter for thermodynamic forcing of $f\text{CO}_2$ rather than $p\text{CO}_2$, as $f\text{CO}_2$ accounts for the non-ideality of CO_2 gas. In the discussion of the updated Takahashi climatology, Tak-2010, we retain the use of $p\text{CO}_{2w}$. Numerically, $f\text{CO}_2 = 0.997 p\text{CO}_2$ at ambient pressure from 4°C to 25°C . Thus, the sea-air $f\text{CO}_2$ difference, $\Delta f\text{CO}_2$, is essentially numerically the same as $\Delta p\text{CO}_2$, such that the results expressed either as $\Delta f\text{CO}_2$ or $\Delta p\text{CO}_2$ can be directly compared. However, determining the sea-air CO_2 flux using $f\text{CO}_{2w}$ and $p\text{CO}_{2a}$ or with $p\text{CO}_{2w}$ and $f\text{CO}_{2a}$ will lead to biases in the global sea-air $f\text{CO}_2$ fluxes of -0.2 PgC yr^{-1} or 0.2 PgC yr^{-1} , respectively.

In the Takahashi $p\text{CO}_2$ climatology, empty cells were filled through interpolation to their neighbors, aided by a modeled surface ocean advection scheme (Bryan & Lewis, 1979). This climatology is extensively used as input or for verification in the different sea-air CO_2 flux products and models. It is chosen here for comparison because it differs from machine learning (ML) and regression schemes in that the $p\text{CO}_{2w}$ observations are interpolated in time and space. This contrasts with the ML and linear regression approaches that use predictor variables to map the surface water fugacity of CO_2 , $f\text{CO}_{2w}$, fields (Rödenbeck et al., 2015). The ML approaches take advantage of the increased number of $f\text{CO}_{2w}$ observations, along with robust fields of predictor variables, to develop time-resolved methods. The $f\text{CO}_{2w}$ maps are created based on a set of predictors, nominally at monthly 1° by 1° resolution (Gregor et al., 2019; Rödenbeck et al., 2015). These scales are in the order of the autocorrelation scales of $f\text{CO}_{2w}$ (Li et al., 2005).

The creation of time-resolved sea-air CO_2 flux densities has focused on approaches to map $f\text{CO}_{2w}$ along with subsequent comparisons and syntheses of the methods (Fay et al., 2021; Gregor et al., 2019; Landschützer et al., 2013; Stamell et al., 2020; Telszewski et al., 2009; Zeng et al., 2014). The RECCAP2 analyses include the output of eleven such approaches with consistent protocols for nomenclature and analysis. The recommended time range for the RECCAP2 surface water analysis spans years from 1985 to 2018. The extremely randomized trees (ET) method described here (AOML-ETv2020) that is used in RECCAP2 covers the period from January 1998 through December 2018. An updated version, AOML-ET-v2023, adds 4 years to the time series, but the results are similar to the AOML-ETv2020 except from 2018 onward. The later start date than the RECCAP2 default of 1985 is chosen because of both the sparsity of $f\text{CO}_{2w}$ data and the lower quality and coverage of predictor variables until the late 90s. Most notably, remotely sensed chlorophyll estimates did not become available from a common source till the end of 1997. The inconsistent predictor variables and lower resolution prior to 1998 likely contribute to the reduced variability in $f\text{CO}_{2w}$ seen during this period for the RECCAP observation-based approaches.

Comparisons of mapped $f\text{CO}_{2w}$ determined by ML approaches and the resulting sea-air CO_2 fluxes use standard indicators such as root mean square error (RMSE), bias, and the ability of the methods to reproduce seasonal and interannual variability and trends at global and basin scales (Rödenbeck et al., 2015). Gloege et al. (2021) showed by using large ensemble model reconstructions of $f\text{CO}_{2w}$ and predictors that ML approaches, when supplied with sufficient data, can skillfully reproduce $f\text{CO}_{2w}$ fields. Regions with fewer $f\text{CO}_{2w}$ observations, such as the Southern Ocean, showed larger errors (Hauck et al., 2023). ML approaches can be enhanced to a modest degree by preprocessing data, such as temperature normalization, which also facilitates deriving the physical-chemical connections between $f\text{CO}_{2w}$ and drivers in ML approaches (Bennington et al., 2022). However, these modifications, choices, and adaptations of predictor variables do not have a significant influence, and statistical indicators are very similar between approaches. This suggests that little improvement in mapping $f\text{CO}_{2w}$ fields is gained in the different ML approaches (Gregor et al., 2019) but that improvements in $f\text{CO}_{2w}$ mapping and regional fluxes can be achieved by more observations and finer resolution (Gregor et al., 2024, accepted; Roobaert et al., 2023). Differences in flux products using other parameters in the bulk flux equation, such as the gas transfer parameterization as well as the sensitivity of the mapped $f\text{CO}_{2w}$ products to different predictor and target variables, have been explored to a lesser extent.

This paper focuses on the impact of temporal atmospheric forcing parameters on sea-air CO_2 fluxes, specifically the factors influencing the magnitudes and trends in $f\text{CO}_{2w}$ and sea-air CO_2 fluxes. The paper is structured as follows: In the methods section, we outline the approach for determining sea-air CO_2 fluxes using the bulk flux formulation. The AOML-ET method is described and expanded in Supporting Information S1 to show it compares well with other approaches, so that the results of applying different atmospheric forcing fields are generally applicable. The comparisons and results are described in terms of the seasonal and regional patterns, using January and July 2010 as representative examples. The seasonal and spatial patterns are compared with an

updated climatology based on the methods of Takahashi et al. (2009), Tak-2010, as submitted to RECCAP2 (de Vries et al., 2023). The effects of changing atmospheric forcing are quantified in three different ways. The mole fraction of CO₂, XCO_{2a}, is used as a predictor instead of time; the fCO_{2w} is replaced by ΔfCO₂ as a target; and a zonally resolved 2-dimensional XCO_{2a} marine boundary layer (MBL) product (time, latitude) is replaced by a 3-dimensional XCO_{2a} field (time, latitude, and longitude) derived from an atmospheric CO₂ transport model, Carbon Tracker (Jacobson et al., 2020). Furthermore, the impact of applying three different gas transfer-wind speed formulations is assessed to illustrate the effect of the kinetic forcing of fluxes that are not considered in the analyses when comparing the correspondence of different sea-air CO₂ flux products. The results largely follow expectations with the exception that replacing fCO_{2w} with ΔfCO₂ as the target causes the decadal ocean CO₂ uptake trend to decrease by 45%. This trend agrees with the consensus value of the trend in ocean CO₂ uptake provided by the Global Carbon Budget.

2. Methodology

2.1. Determination of Sea-Air CO₂ Flux Densities

Sea-air CO₂ flux densities are commonly expressed in terms of a bulk flux formulation that requires knowledge of fCO_{2w} along with CO₂ air concentrations and the rate of CO₂ transfer across the sea-air interface:

$$F_{sa} = \overline{k K_0 (fCO_{2w} - fCO_{2a})} = \overline{k K_0 \Delta fCO_2} \quad (1)$$

where F_{sa} is the flux density with positive values depicting effluxes. k is the gas transfer velocity, and K_0 is the solubility of CO₂ in seawater. The overbar depicts the temporally integrated quantity.

In practice, when calculating flux densities, the monthly ΔfCO₂ fields at 1° by 1° grid are multiplied by the product of gas transfer velocity and solubility, thereby expressing F_{sa} as:

$$F_{sa} = \overline{k K_0 \Delta fCO_2} \quad (2)$$

The Taylor expansion from the average of the product (Equation 1) to averages of the individual terms has cross-correlation terms of k' and $\Delta fCO_2'$, but these terms have been shown to have a small influence on the overall results for determination of monthly flux densities on scales of 1° (Wanninkhof et al., 2011) and are not included here. The ΔfCO₂ is determined from fCO_{2w} at 1–6 m below the interface (fCO_{2w}) and air (fCO_{2a}) at monthly scales and 1° by 1° resolution. fCO_{2a} is derived from a zonally averaged time series of mole fraction XCO_{2a} of the MBL, abbreviated as MBL-RS (Dlugokencky et al., 2021).

k is commonly parameterized as the square of wind speed (Wanninkhof et al., 2009):

$$k = 0.251 \langle u^2 \rangle (Sc/660)^{-1/2} \text{ or } k_{660} = 0.251 \langle u^2 \rangle \quad (3)$$

where $\langle u^2 \rangle$ is the second moment of the wind at 10-m height and is calculated here from 6-hourly winds at ¼° resolution (Hersbach et al., 2020). Sc is the Schmidt number determined from temperature and salinity (Wanninkhof, 2014), and 660 is the Schmidt number of CO₂ at 20°C where $k_{660} = k (Sc/660)^{1/2}$. The coefficient 0.251 is obtained by scaling the gas transfer-wind speed relationship to the global average of the second moment of the wind as derived from the European reanalysis product (ERA5) and the inventory of bomb ¹⁴C in the ocean (Sweeney et al., 2007). In Equation 3, k has units of cm hr⁻¹ and $\langle u^2 \rangle$ is expressed as m² s⁻².

The flux densities F_{sa} (mol m⁻² yr⁻¹) are aggregated into regional or global fluxes, with the flux expressed as peta-gram carbon per year, PgC yr⁻¹, where a Pg equals 10¹⁵ g. In the terrestrial and atmospheric carbon cycle studies, bulk fluxes are often expressed as Pg of CO₂ yr⁻¹, where 1 PgCO₂ equals 0.27 PgC. In the RECCAP2 protocol and several other global studies, the sea-air CO₂ fluxes are positive if the net flux is into the ocean (influx or uptake), while for oceanographic applications and in this manuscript, the flux into the ocean is presented as a negative value. A summary of the sources of variables used and the differences in conventions between RECCAP2 and this work are provided in Table S1 in Supporting Information S1.

2.2. AOML-ET $f\text{CO}_{2w}$ Gap Filling Methodology

The AOML-ET is one of eleven ML and regression approaches that use the same community-assembled SOCAT database (Bakker et al., 2016) to map $f\text{CO}_{2w}$ in RECCAP2. The extremely randomized trees, ET, methodology is an adaptation of the Random Forest approach that has been applied in regional ocean carbon flux mapping. It has shown similar skill to other approaches used to create $f\text{CO}_{2w}$ fields (Chen et al., 2019; Gregor et al., 2017; Sharp et al., 2022; Wu et al., 2024). The ET ML algorithm is detailed in Geurts et al. (2006), and specifics of the AOML-ET adaptation are provided in Supporting Information S1. In short, it is based on a decision tree approach, and its training uses a tree-based ensemble where nodes are split at random cut points using all observations to build the model. The hyperparameters in the model are optimized with regard to branches and cut points to balance minimizing differences between test data and results and avoiding overfitting. The ET method is computationally efficient and lends itself to exploration of the impact of different variables. Potential drawbacks of the ET method include that it can be more prone to bias in data-sparse regions and at the start and end of the time series, or tail effects, compared to other ML methods. More specifically, with the ET approach, observations in regions with few data are viewed as outliers such that adjacent data further removed in time and space receive greater weight (Gregor et al., 2019). It also has greater sensitivity to overfitting compared to other ML approaches (Gregor et al., 2019; Stamell et al., 2020).

The data set used for training AOML-ETv2020 and other ML approaches in RECCAP2 is the SOCATv2020 product, which includes over 33 million unique $f\text{CO}_{2w}$ observations collected from 1957 through 2019 (www.socat.info). However, for AOML-ET and all other ML analyses, the gridded SOCAT data product is used, which consists of data collated into monthly 1° by 1° cells, reducing the total to approximately 277 thousand $f\text{CO}_{2w}$ data points. The AOML-ET was extended after the RECCAP2 analysis with $f\text{CO}_{2w}$ observations through 2022. This product is referred to as AOML-ETv2023. This analysis used the gridded SOCATv2023 data comprised of 317 thousand cells. Remote areas of the oceans and winter seasons in the mid- and high-latitude oceans have few $f\text{CO}_{2w}$ observations and are thus reliant on gap filling with predictors. Predictor variables for the default configuration AOML-ET are monthly 1° by 1° gridded products of sea surface temperature (SST), sea surface salinity (SSS), chlorophyll-a (Chl-a), and mixed layer depths (MLD), with their sources provided in Table S1 in Supporting Information S1. These variables are known to directly influence $f\text{CO}_{2w}$ through biogeochemical and physical interactions that control $f\text{CO}_{2w}$. Location (latitude, longitude) and time (month since October 1997) are included in the AOML-ET method to facilitate the depiction of regional variations and trends. Training and mapping in some ML and regression approaches are facilitated by delineation of regions into specific biogeographical provinces or biomes (e.g., Fay & McKinley, 2014) and/or removing the direct temperature impact on $f\text{CO}_{2w}$ (Bennington et al., 2022) but are not applied to AOML-ET.

At monthly 1° by 1° grid spacing, there are 11.3 M possible grid nodes from October 1997 through December 2020, and about 2% of the monthly 1° by 1° cells have $f\text{CO}_{2w}$ observations (Stamell et al., 2020). Even for the best sampled months, only a small fraction have $f\text{CO}_{2w}$ observations in the gridded SOCATv2020 product. The highest coverage is for August 2011 and encompasses 4.3% of all cells. For AOML-ET, 70% of the data are placed into a training data set, and 30% are reserved for the testing data set to determine bias, variability, and uncertainty of the mapped products. Testing data include all the $f\text{CO}_{2w}$ observations from years 2000, 2005, 2010, and 2015. For AOML-ETv2023, an additional year, 2018, is withheld from training for testing. Omitting data from whole years is preferable to randomly withholding data points for testing since this could lead to favoring test data in well-sampled areas and seasons, causing uncertainty to not be appropriately represented. To determine the efficacy of the approaches and to assess overfitting, runs were performed where the entire data set was used for training without withholding test data, which negates the ability to assess the performance. As shown in Supporting Information S1, only small differences were observed, suggesting that on the global scale, the default AOML-ET approach has an appropriate set of predictors and hyperparameters.

2.3. The Takahashi 2010 Climatology

To investigate seasonal and regional differences in sea-air CO_2 fluxes between approaches, a comparison is made between the AOML-ET output for 2010 and the updated monthly Takahashi climatology centered on 2010 (Tak-2010) created on a native resolution of a 4° by 5° grid and subsequently sub-gridded to 1° resolution as submitted to RECCAP2 (Müller, 2023). This monthly climatology is the authoritative benchmark for air-sea CO_2 fluxes and is used as a predictor in some ML techniques (Landschützer et al., 2016). The creation of Tak-2010 follows the

same procedures as the previous climatology centered on the year 2000 (Takahashi et al., 2009). Tak-2010 uses the SOCATv2020 data set to determine $p\text{CO}_{2w}$ like in the AOML-ETv2020 analysis, except that the $p\text{CO}_{2w}$ is mapped on a monthly 4° by 5° grid. In Tak-2010, the $p\text{CO}_{2w}$ values are adjusted to 2010 by assuming that $p\text{CO}_{2w}$ increases at a discretized rate tied to XCO_{2a} increase. Therefore, for $p\text{CO}_{2w}$ data between 1957 and 1979, $1 \mu\text{atm yr}^{-1}$ was added to each $p\text{CO}_{2w}$ observation; for 1980 through 2000, $1.5 \mu\text{atm yr}^{-1}$ was added; from 2001 through 2009, $2 \mu\text{atm yr}^{-1}$ was added; and between 2011 and 2018, $2 \mu\text{atm yr}^{-1}$ was subtracted to normalize the $p\text{CO}_{2w}$ to the virtual year of 2010. The climatological XCO_{2a} , P, and SST values for 2010 were used in the creation of flux maps. The Tak-2010 climatology was recently updated by Fay et al. (2024) using a slightly different approach for accounting for the atmospheric forcing and associated $f\text{CO}_{2w}$ increases through time by assuming that the surface ocean tracks the global atmospheric XCO_{2a} increase exactly on annual scales. As the assumptions on XCO_2 increase are similar and only used to normalize the $p\text{CO}_{2w}$ observations to a common year, the results show the same monthly spatial patterns. The Fay et al. (2024) analysis yields a global flux of $-1.79 \pm 0.70 \text{ PgC}$ in close agreement with Tak-2010 results presented here of $-1.86 \pm 0.52 \text{ PgC}$ for 2010.

2.4. Sensitivity of Sea-Air CO_2 Fluxes to Different Atmospheric Forcing Input Variables

Several adaptations to the AOML-ET default configuration are implemented to assess sensitivity to procedures and predictor variables with a focus on atmospheric forcing. The default configuration of AOML-ET uses location, time, SST, SSS, MLD, and Chl-a as predictors and $f\text{CO}_{2w}$ as the target in the training step. The changes include using XCO_{2a} instead of month as a predictor and using $\Delta f\text{CO}_2$ as target instead of $f\text{CO}_{2w}$. In Supporting Information S1, the results are shown of adding and deleting select predictor variables for training of AOML-ET with Chl-a and MLD being omitted and adding $\langle u^2 \rangle$ as a predictor. As detailed below, most of the adaptations did not yield significant differences on global scales, with the notable exception of substituting the target $f\text{CO}_{2w}$ for $\Delta f\text{CO}_2$.

All ML methods, including AOML-ET, are used to map $f\text{CO}_{2w}$ fields, while the sea-air CO_2 flux is a function of the thermodynamic forcing, $\Delta f\text{CO}_2$ (Equation 2). To assess if mapping $f\text{CO}_{2w}$ and then subtracting $f\text{CO}_{2a}$ to determine $\Delta f\text{CO}_2$ versus predicting and mapping $\Delta f\text{CO}_2$ directly has an influence on fluxes, AOML-ET was trained with $\Delta f\text{CO}_2$ as the target variable. The $\Delta f\text{CO}_2$ for the training step was calculated from the monthly 1° by 1° gridded $f\text{CO}_{2w}$ fields and subtracted from $f\text{CO}_{2a}$ determined from the MBL-RS XCO_2 product (Equation 4).

In addition to investigating factors that impact the mapping of the monthly $f\text{CO}_{2w}$ fields with AOML-ET, different k and XCO_{2a} products are used to determine their influence on flux densities (Equation 2). The effect of using a 3-dimensional XCO_{2a} product is quantified to show how regional differences in XCO_{2a} will impact fluxes (Wanninkhof et al., 2019). In most analyses to date and in the RECCAP2 protocol, XCO_{2a} values from the MBL-RS are used, with XCO_{2a} samples taken weekly at 60 sites around the globe forming the basis of this product (https://gml.noaa.gov/ccgg/about/global_means.html, Dlugokencky et al., 2021). In this zonally invariant MBL-RS product, the XCO_{2a} is expressed with time and latitude. To match the $f\text{CO}_{2w}$ resolution, this XCO_{2a} data is re-gridded on a monthly 1° by 1° grid and used to calculate $f\text{CO}_{2a}$ through

$$f\text{CO}_{2a} = G_f(T, S) (P - p\text{H}_2\text{O}) \text{XCO}_{2a} \quad (4)$$

where P is the barometric pressure at sea level, $G_f(T, S)$ is the fugacity correction ($=0.996$ from 0°C to 25°C), and $p\text{H}_2\text{O}$ is the saturation water vapor pressure calculated from P and SST (Pierrot et al., 2009) on the monthly 1° by 1° grid.

The default MBL-RS product is compared with a XCO_{2a} distribution over the ocean surface derived from an assimilation scheme, CarbonTracker CT2019B (Jacobson et al., 2020). CT2019B provides a spatially and temporally varying representation of XCO_{2a} throughout the troposphere created by assimilating a wide variety of atmospheric CO_2 data in a 3-D atmospheric chemistry-transport model, TM5 (Krol et al., 2005). This CT-PBL product provides XCO_{2a} globally at 3-hourly intervals and at 3° longitude by 2° latitude spanning 2000–2020. The PBL height in TM5 is estimated from the ERA5 meteorology and a bulk Richardson number formulation (Jacobson and Munro, pers. com.), where the XCO_{2a} for the layers within the PBL is averaged. Subsequently, the 3° longitude by 2° latitude bins are re-gridded to a 1° by 1° grid and averaged monthly to determine the $f\text{CO}_{2a}$ (Equation 4) and the flux density (Equation 2). The CT-PBL product covers the time span from 2000 to 2020, and

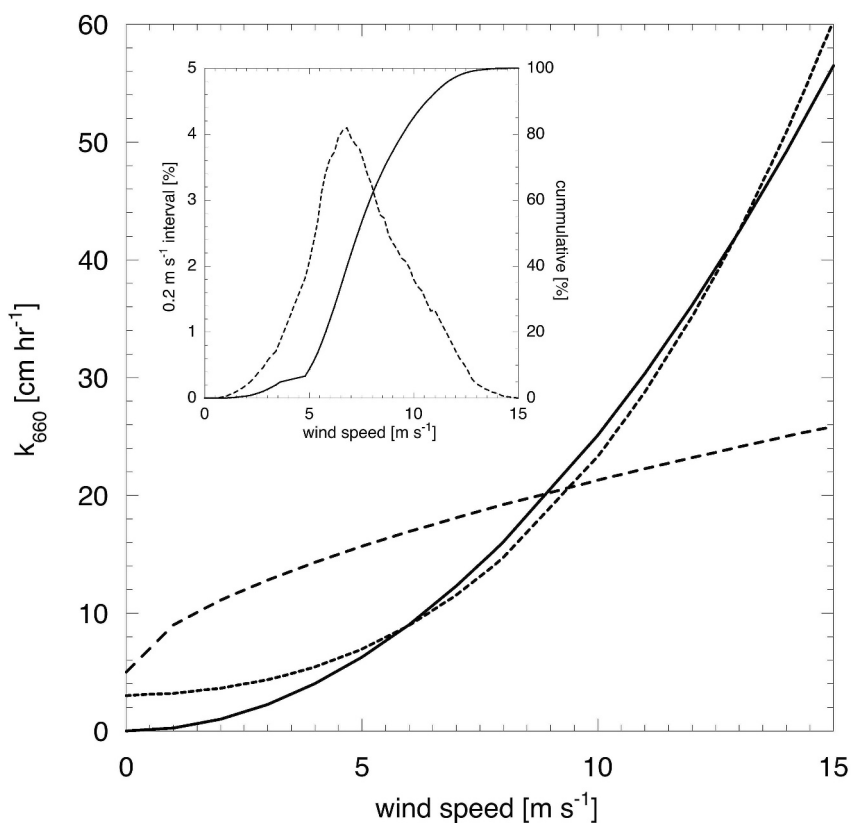


Figure 2. The canonical dependence of gas transfer with the square of the windspeed, $k_{660} = 0.251 \langle u^2 \rangle$ (solid line); a hybrid dependence, $k_{660} = 3 + 0.1 \langle u \rangle + 0.083 \langle u^2 \rangle + 0.011 \langle u^3 \rangle$ (dashed line); and a relationship meeting global isotopic constraints, $k_{660} = 5 + 4 \langle u^{0.61} \rangle$ (long dashed line). Inset, global windspeed distribution (dashed line, left axis) and cumulative distribution (solid line, right axis) at 0.2 m s^{-1} intervals.

we use AOML_ETv2023 in the analysis to avoid tail effects of AOML_ETv2020 after 2018 (see Supporting Information S1).

Three different gas exchange parameterizations that differ in their assumptions of kinetic forcing are used to determine the effect on the global sea-air CO_2 fluxes. The default is a quadratic dependence with zero intercept (Equation 3). The second expression is a hybrid parameterization with a cubic dependency with wind and a non-zero intercept:

$$k_{660} = 3 + 0.1 \langle u_{10} \rangle + 0.083 \langle u_{10}^2 \rangle + 0.011 \langle u_{10}^3 \rangle \quad (5)$$

The coefficient for the second moment of the wind has been adjusted in Equation 5 from 0.064 in the original equation of Wanninkhof et al. (2009) to 0.083 to account for the different wind fields used between the original work and here.

The third choice is that presented in Krakauer et al. (2006), using the isotopic constraints ^{13}C and ^{14}C and an ocean circulation model that yields a low exponent for wind speed. Tuning this to a global average gas transfer rate based on bomb- ^{14}C following Sweeney et al. (2007) yields an equation of

$$k_{660} = 5 + 4 \langle u^{0.61} \rangle \quad (6)$$

The parameterizations are shown versus wind speed in Figure 2. Equation 6 has a significantly different behavior with wind, although it is constrained in a similar fashion as the quadratic and hybrid parameterizations.

The effect of different wind speed products on global sea-air CO_2 fluxes has been detailed in Roobaert et al. (2018). At a global scale, the differences in wind speed can be mitigated through normalization of the wind

products and gas transfer-wind speed dependencies. The normalization is done by adjusting the coefficients in the relationships to a global average wind speed and gas transfer velocity value (Fay et al., 2021) that are constrained by global bomb- ^{14}C inventories. The rationale behind quadratic and hybrid relationships (Equations 3 and 5) is based on the controls of gas transfer at the interface as described in Wanninkhof et al. (2009). The isotopic constraint does not include inferences of processes controlling gas transfer but relies on cost functions of ^{13}C and ^{14}C measurements in the ocean in conjunction with an ocean transport model. While the range of solutions provided in Krakauer et al. (2006) is broad, they all have a low exponent for wind speed, resulting in a weak dependency of gas transfer with wind.

3. Results and Discussion

Much of the work quantifying variability and trends in sea-air CO_2 fluxes has focused on mapping surface water fugacity ($f\text{CO}_{2w}$), as $f\text{CO}_{2w}$ is a primary driver of fluxes. The AOML-ET method is used here to examine how different atmospheric forcing parameters impact both $f\text{CO}_{2w}$ and sea-air CO_2 fluxes. These results demonstrate that factors other than $f\text{CO}_{2w}$, particularly on regional scales, can have a significant influence on the fluxes.

Comparisons of various ML approaches reveal that the global trends in sea-air CO_2 fluxes for many methods are correlated with initial conditions, suggesting that these conditions contribute to differences in trends. On a global scale, the salient features of the mapped $f\text{CO}_{2w}$ fields from ML methods using the common SOCAT observational data set are very similar. Therefore, the method of gap filling does not significantly influence global $f\text{CO}_{2w}$ spatial patterns. This aligns with the findings of Gregor et al. (2019), who showed that uncertainties in global fluxes due to different gap-filling approaches were similar. However, regional differences, especially near the coast (see, for example, Figure S1 in Wu et al., 2024), as well as the magnitude and trends of sea-air CO_2 fluxes, are more sensitive to the methodology.

Assessing the fidelity of ML approaches beyond comparisons and statistical analysis is challenging, as these methods function as “black boxes.” To address this, we assess the sensitivity of the global sea-air CO_2 flux to different predictor and target variables. This is done through feature importance analysis, changing targets, and withholding predictors using the AOML-ET method.

3.1. Global and Regional Patterns of Trends in Fluxes Using the AOML-ET Method

The interannual variability and trends in global sea-air CO_2 fluxes from 1998 to 2020, as determined by the AOML-ETv2020 method, show good correspondence with other products used in the RECCAP2 and GCB_2022 analyses. All methods show a minimum in CO_2 uptake around 2000 followed by an increasing negative trend. There is convergence in the magnitude of uptake for the different approaches during the middle part of the record, with particularly good agreement from 2009 to 2014. This period coincides with the highest observational data density and fewer issues related to tail effects, which can cause divergence at the beginning and end of the time series.

The magnitude of the flux at the beginning of the time series influences the trend, with a lower flux resulting in a stronger negative trend (Figure 3). AOML-ETv2020 shows a more negative global trend of $-0.89 \text{ PgC yr}^{-1} \text{ decade}^{-1}$ compared to other methods, which show an average trend of $-0.7 \text{ PgC yr}^{-1} \text{ decade}^{-1}$, ranging from $-0.5 \text{ PgC yr}^{-1} \text{ decade}^{-1}$ to $-0.8 \text{ PgC yr}^{-1} \text{ decade}^{-1}$ over the 1998–2020 period (Figure 1, Table 1). The larger negative trend for AOML-ETv2020 is attributed to the low CO_2 uptake at the beginning of the time series and the strong feedback of increasing CO_2 fluxes due to rising $\Delta f\text{CO}_2$. A smaller initial uptake and increasing XCO_{2a} values over time create a larger disequilibrium, which subsequently increases uptake later in the period. This feedback is reflected in the strong correlation between global sea-air CO_2 flux and the global average $\Delta f\text{CO}_2$ (Figure 4).

For the first part of the time series (1998–2009), AOML-ETv2020 shows a trend of $-1.22 \text{ PgC yr}^{-1} \text{ decade}^{-1}$, while from 2010 to 2020, the trend slows to $-0.64 \text{ PgC yr}^{-1} \text{ decade}^{-1}$. The lower uptake in AOML-ETv2020 compared to other methods at the start of the record (1998–2001) may be due to anomalous oceanic conditions associated with the 1998 El Niño and the subsequent hiatus in global warming (1998–2012) (Liu & Xie, 2018). These conditions likely affected external forcing (McKinley et al., 2020), having a larger effect on AOML-ET's training than on other models. This is particularly due to the fact that AOML-ET's predictor data starts in 1998, whereas other methods begin in 1985.

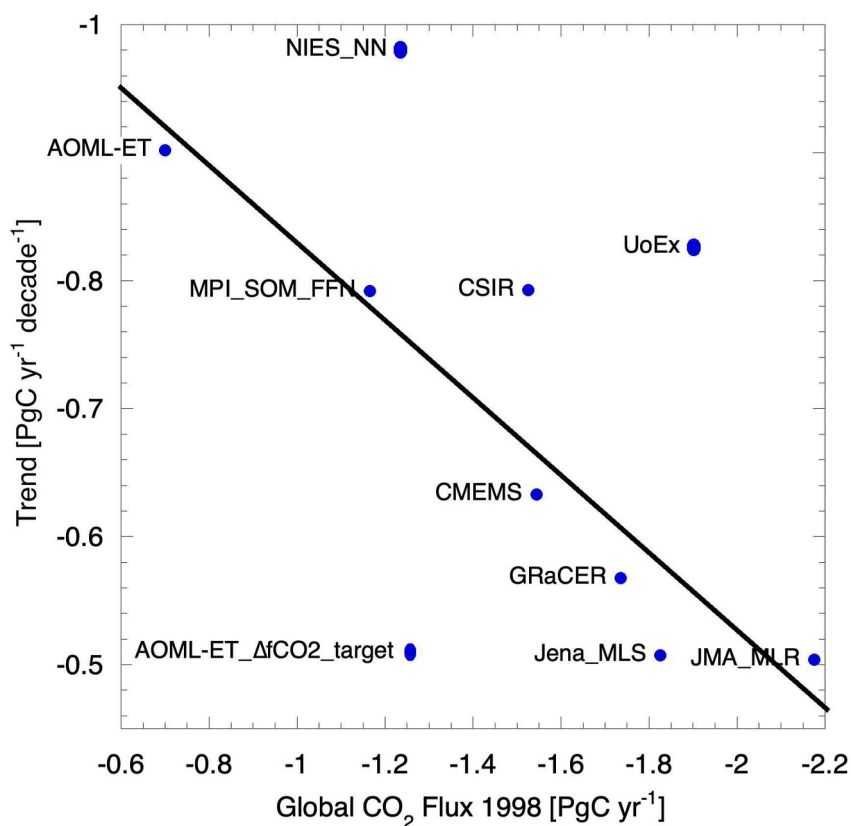


Figure 3. Relationship between global ocean CO₂ uptake in 1998 and the trend from 1998 to 2020 for different ML methods. The linear relationship plotted ($\text{Trend [PgC yr}^{-2}] = 0.11 - 0.03 \text{ Flux 1998}$, $r^2 = 0.84$) does not include the ML approaches of the AOML-ET_dfCO₂ target, NIESS-NN, and UoEx. For references to the methods, see the caption in Table 1.

The seasonal and regional patterns determined by AOML_ET are consistent with the Tak-2010 climatology for 2010. Representative flux density maps for AOML-ET for January and July 2010 illustrate spatial and seasonal patterns in flux densities (Figure 5). There is outgassing in tropical oceans and upwelling regions, while subtropical and subpolar areas exhibit CO₂ uptake. Subtropical regions transition from strong sinks in winter to sources in summer, primarily driven by changes in sea surface temperature (SST). In the Bering Sea, a strong winter source contrasts with other Northern high-latitude regions, which are weak wintertime sinks. This region also shows a different trend in flux and an anomalously low increase in fCO_{2w} over time (Takahashi et al., 2009), which is attributed to deepening of the mixed layer in winter that entrains high-CO₂ waters. Overall, winter shows greater CO₂ uptake than summer in the respective hemispheres, driven by cooling in the subtropical gyres and associated temperature-driven CO₂ uptake. Globally, the greatest CO₂ uptake occurs between December and March.

Figure 6 presents a Taylor diagram summarizing key statistics for AOML-ET. The diagram quantifies the correspondence between the output of AOML-ET and the test data, which are comprised of the observations in 2000, 2005, 2010, and 2015, in terms of correlation coefficient, root mean square error (RMSE), and standard deviation. For AOML-ETv2020, the correlation coefficient (r^2) is 0.83, with an RMSE of 17 μatm , aligning with other ML and regression estimates (Gregor et al., 2019; Rödenbeck et al., 2015). The standard deviation, which represents variability, is 34 μatm , compared to 43 μatm for the test data. This suggests that, like other ML methods, AOML-ET does not capture the full range of variability, in part due to the relatively coarse grid and monthly time scale used (Gregor et al., 2019). For example, Gregor et al. (2024) increased the resolution to an 8-day, $\frac{1}{4}^\circ$ scale in their ML analysis and observed a 15% increase in variability, indicating that variability is sensitive to temporal and spatial scales. However, scaling to finer resolutions is often limited by the lack of predictor variables at comparable resolutions.

Table 1
Summary of Magnitude Variability and Trends of Global Sea-Air CO₂ Fluxes From Different Machine Learning Approaches

Study ^a	Average 1998–2020 ^b PgC yr ⁻¹	Trend ^c PgC yr ⁻¹ decade ⁻¹	r ² ^d	StError ^e PgC yr ⁻¹	Flux 1998 ^f PgC yr ⁻¹	Flux 2020 ^g PgCyr ⁻¹
AOML-ET	-1.70	-0.89	0.92	0.19	-0.72	-2.54
<i>AOML-ET-Chl-a</i>	<i>-1.82</i>	<i>-0.87</i>	<i>0.86</i>	<i>0.24</i>	<i>-0.71</i>	<i>-2.33</i>
<i>AOML-ET-MLD</i>	<i>-1.72</i>	<i>-0.87</i>	<i>0.88</i>	<i>0.23</i>	<i>-0.80</i>	<i>-2.28</i>
<i>AOML-ET+<U²></i>	<i>-1.72</i>	<i>-0.94</i>	<i>0.93</i>	<i>0.17</i>	<i>-0.71</i>	<i>-2.72</i>
<i>AOML-ET_ΔfCO₂</i>	<i>-1.65</i>	<i>-0.51</i>	<i>0.91</i>	<i>0.11</i>	<i>-1.28</i>	<i>-1.99</i>
MPI-SOMFFN	-1.91	-0.79	0.93	0.15	-1.17	-2.56
Jena-MLS	-1.99	-0.51	0.63	0.26	-1.83	-2.60
CMEMS	-1.94	-0.63	0.92	0.13	-1.54	-2.88
GRaCER	-2.12	-0.57	0.95	0.09	-1.74	-2.66
JMA-MLR	-2.36	-0.50	0.77	0.19	-2.18	-3.25
NIES_NN	-2.01	-0.98	0.93	0.18	-1.24	-3.42
CSIR	-2.08	-0.79	0.96	0.11	-1.53	-3.02
UoEx	-2.43	-0.83	0.92	0.17	-1.90	-2.89
Average ^h	-2.06	-0.7	0.88	0.16	-1.53	-2.87
Min. ^h	-1.70	-0.5	0.63	0.09	-0.70	-2.54
Max. ^h	-2.43	-0.98	0.96	0.26	-2.18	-3.42

^aAll data, except AOML-ET, are from <https://globalcarbonbudget.org/carbonbudget/>. AOML_ETv2020 (this work); MPI-SOMFFN (Landschützer et al., 2016); Jena-MLS (Rödenbeck et al., 2022); CMEMS (Chau et al., 2022); GRaCER (Gregor & Gruber, 2021); NIES_NN (Zeng et al., 2014); JMA-MLR (Iida et al., 2021); CSIR (Gregor et al., 2019); UoEx (Watson et al., 2020). ^bTwenty-three-year average (1998–2020) of the annual global values for each approach in PgC yr⁻¹. ^cTrend based on a linear regression of the twenty-three years of annual global sea-air CO₂ fluxes in PgC yr⁻¹ decade⁻¹. ^dCoefficient of determination. ^eStandard error from the linear trend. ^fGlobal sea-air CO₂ flux in 1998 for each of the methods. ^gGlobal sea-air CO₂ flux in 2020 for each of the methods. ^hAverage, minimum, and maximum of the methods (listed in bold) excluding the permutations of AOML-ET (in italics).

Regional trends in the AOML-ET fluxes from 1998 to 2020 reveal significant variability. These regional anomalies in trends are shown relative to the global mean trend of $-0.173 \text{ mol m}^{-2} \text{ yr}^{-1} \text{ decade}^{-1}$ in Figure 7. Most areas with large trend anomalies (Figure 7a) have *P*-values less than 0.01, indicating high statistical significance (Figure 7b). Regions with increasing CO₂ uptake or less outgassing are those with negative anomalies in trends. This is primarily due to rising atmospheric CO₂ levels and oceanic fCO_{2w} not keeping pace with this rise. Negative anomalies in trends are most prominent in high-latitude, seasonally stratified regions, which serve as conduits to the deep ocean. In contrast, neutral and positive regional trends—indicating decreased uptake or increased outgassing over time—are seen in mid- and low-latitude regions. These trends can be attributed to rising SSTs and possible decreases in biological productivity (Landschützer et al., 2018). Changing circulation patterns contribute to smaller negative trends, as observed, for example, in the Western Equatorial Pacific (Ishii et al., 2020).

Broadly, the regional trends align with observation-based analyses of fCO_{2w} trends by Fay and McKinley (2013). Their analysis suggests that regions with greater increases in fCO_{2w} relative to atmospheric increases correspond to areas with rising SSTs. They also show that regions with deep (winter) mixed layers experience smaller increases in fCO_{2w}, which corresponds to areas showing increasing negative flux trends in our analysis. In summary, the trends shown in AOML-ETv2020 fluxes indicate a large-scale shift in ocean uptake patterns, with high-latitude regions becoming stronger sinks and subtropical sinks decreasing in magnitude or becoming sources over the past two decades.

3.2. AOML-ET Global and Regional Fluxes Compared to the Takahashi Climatology for 2010

The AOML-ETv2020 fluxes in 2010, compared to the Tak-2010 climatological fluxes centered on 2010, show similar magnitudes and patterns once normalized for surface area. Specifically, the global fluxes in Tak-2010 are

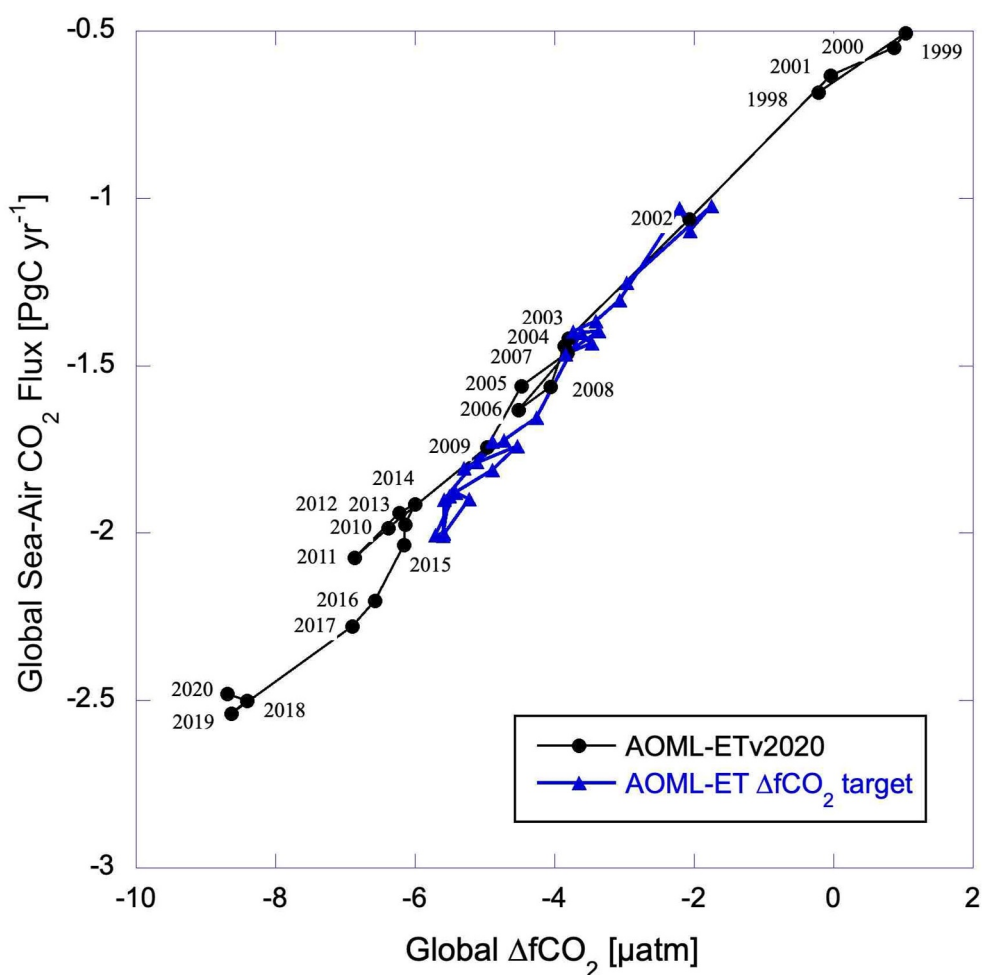


Figure 4. Global sea-air CO₂ flux for the default AOML-ETv2020 approach versus global average ΔfCO₂ with years listed (black circles) and for the AOML-ETv2020 using ΔfCO₂ as a target (blue triangles). The regression between net flux and ΔfCO₂ is 0.214 PgC yr⁻¹ μatm⁻¹ ($r^2 = 0.99$) for AOML-ETv2020 and 0.254 PgC yr⁻¹ μatm⁻¹ ($r^2 = 0.98$) for the AOML-ETv2020_ΔfCO₂ target.

scaled by 1.15 to account for the smaller ocean area covered. The global average sea-air CO₂ fluxes and monthly variability, expressed as the standard deviation of the monthly values in 2010, are -2.03 ± 0.46 PgC yr⁻¹ and -1.86 ± 0.52 PgC yr⁻¹ for the AOML-ETv2020 and Tak-2010, respectively.

The monthly fluxes of the two products are compared in Figure 8 for the zones delineated in Takahashi et al. (2009). Both products show the greatest uptake of 0.2 PgC month⁻¹ from November through March and the smallest uptake of about 0.1 PgC month⁻¹ in August (Figures 8a and 8b). Overall, the differences in global monthly uptake between products are small (less than 0.05 PgC month⁻¹), with the largest differences in February and March. The tropical regions (14°S–14°N) exhibit persistent outgassing throughout the year in both products, though Tak-2010 shows greater outgassing during the boreal spring and summer compared to AOML-ETv2020. This is partly attributed to Tak-2010 not capturing interannual variability, such as El Niño events. Thus, AOML-ET reflects lower outgassing in the 14°N to 14°S band during the boreal spring of 2010 when El Niño conditions prevailed, but this is not reflected in Tak-2010, which excludes data from the Equatorial Pacific during El Niño years. In contrast, during the latter part of 2010, which was dominated by La Niña conditions, fluxes in the tropics are very similar between products (Figures 8a and 8b).

For other regions, both products show that the 50°N to 14°N and 50°S to 14°S latitude bands are generally sinks, with greater uptake in winter for both products in their respective hemispheres. The 50°N to 14°N latitude band in Tak-2010, however, shows small effluxes, whereas AOML-ET shows a small sink from July through September.

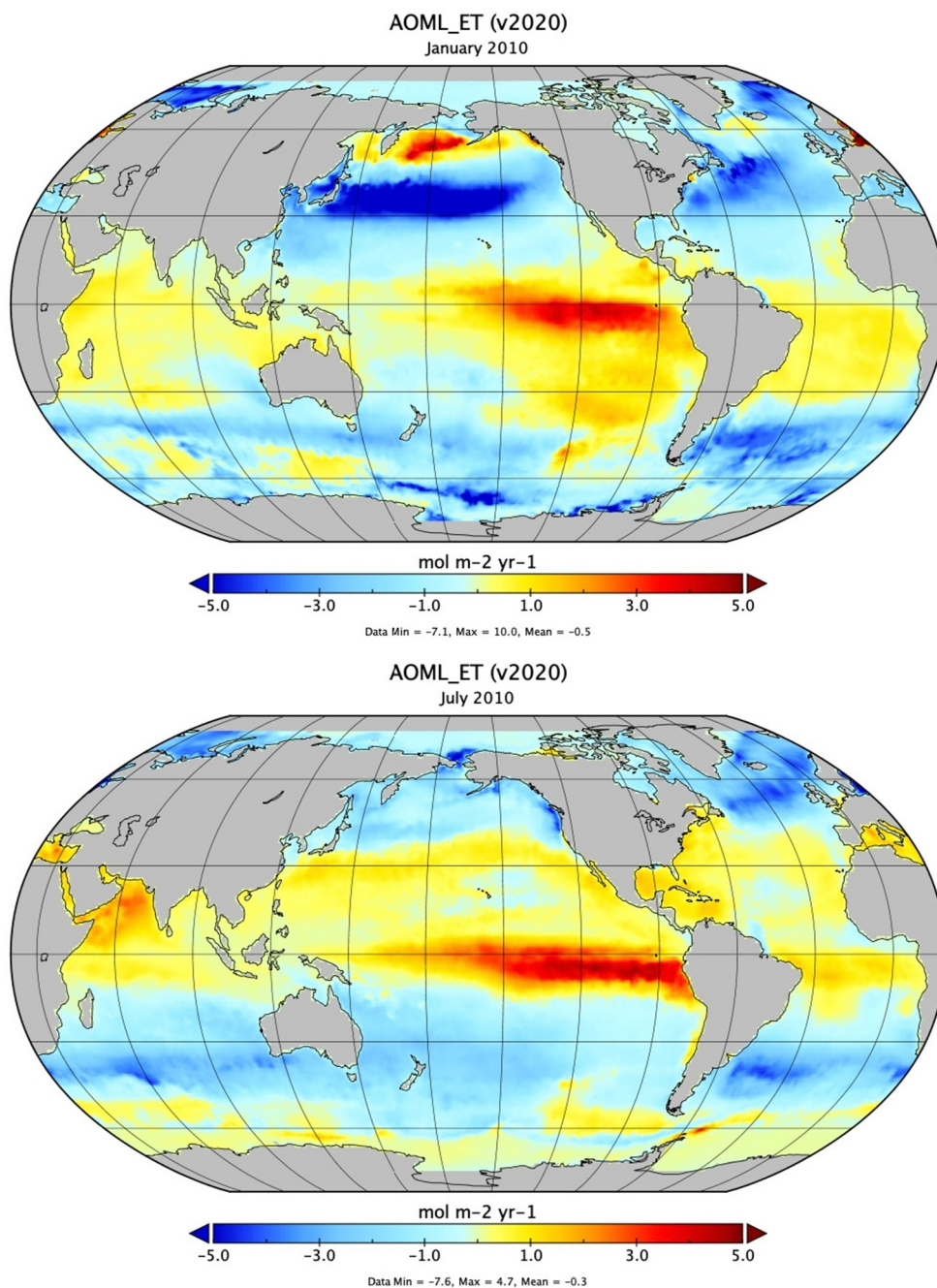


Figure 5. Flux density maps for January (a) and July (b) 2010 using AOML-ET provide a visual depiction of spatial variation in flux for 2010. The color bar has units of units mol m⁻² yr⁻¹.

The high latitudes (>50°N/S) are persistent sinks with large negative fluxes in summer, which align with increased biological productivity that draws down the fCO_{2w} (Takahashi et al., 2009). In the seasonal ice zone (>62°S), wintertime uptake is negligible due to ice cover inhibiting gas exchange.

The monthly zonal differences in fluxes between AOML-ET in 2010 and Tak-2010 (Figure 8c) are attributed to the gap-filling method applied to the fCO_{2w} values, as the gas transfer velocities and fCO_{2a} used for both products are the same. Despite some regional differences, the global fluxes are within ±0.08 PgC month⁻¹. These differences are temporally and zonally compensating, with adjacent regions showing both positive and negative differences, which partially offset each other. For instance, in the 14°N–50°N zonal band, which is an uptake

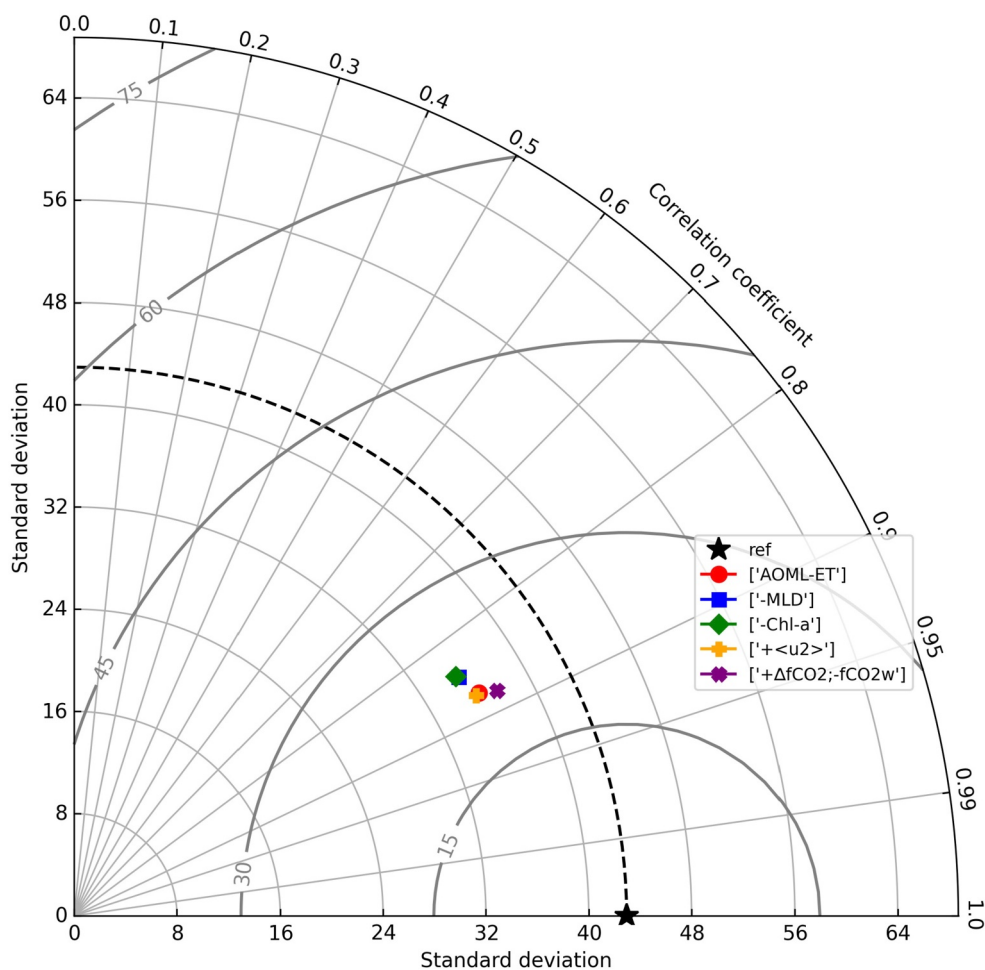


Figure 6. Taylor diagram of the fCO_{2w} values determined by AOML-ET values compared with the test data for the permutations listed in Figure 9 and Figure S1 in Supporting Information S1. The test data is shown as a black star. The red circle is AOML_ETv2020 in default configuration; the blue square is AOML_ET without MLD as a predictor; the green diamond is the AOML_ET without Chl-a as a predictor; the yellow plus symbol shows the addition of $\langle u^2 \rangle$; and the green cross is the output replacing fCO_{2w} by ΔfCO_2 as target. The Pearson correlation coefficient is shown on the arc, the standard deviation indicating variability is provided on the axes, and the semi-circles show the RMSE.

region for much of the year, AOML-ET shows less uptake compared to Tak-2010. From July through September, the region outgasses both products, but with greater outgassing in Tak-2010. Spatial compensation is also evident, with differences between 15°S and 50°S largely counteracted by opposing changes in the northern regions (Figure 8c).

The subpolar divergence zone and marginal ice zones in the Southern Hemisphere, represented by the bands from 50°S–62°S and >62°S, are under-sampled regions with differing results in the analyses. This region is thought to represent a CO_2 source based on fCO_{2w} calculations from pH sensors on profiling floats and estimated alkalinity (Bushinsky et al., 2019; Gray et al., 2018). Data from these regions, particularly in winter, are sparse in the SOCAT database, so the flux values in these areas are largely dependent on gap-filling methods. Both Tak-2010 and AOML-ET in 2010 show strong uptake in the summer months (November–March) and less uptake in winter. However, the subpolar divergence zone in Tak-2010 shows outgassing, while AOML-ET indicates a weak sink in winter. This difference may arise because Takahashi et al. (2009) show a strong correlation between fCO_{2w} and the day of year in waters colder than $-1.75^\circ C$, with wintertime fCO_{2w} values higher than fCO_{2a} . This suggests that the training data for AOML-ET in this region may be insufficient, and the climatological interpolation in Tak-2010 provides a better representation. Overall, despite differences in data utilization and gap-filling approaches,

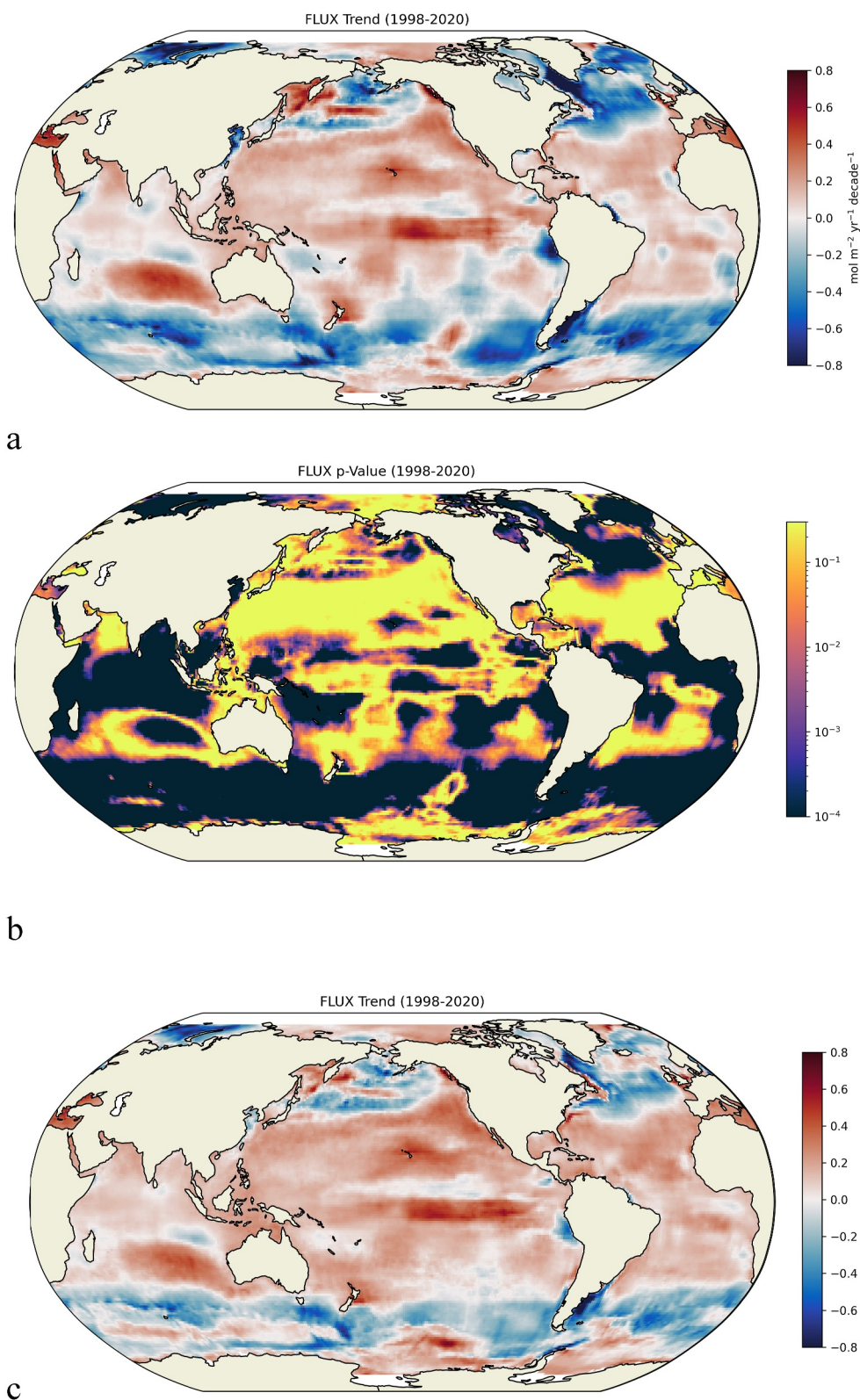


Figure 7. (a) Map of regional trends in sea-air CO₂ flux densities from 1998 to 2020 in mol m⁻² yr⁻¹ decade⁻¹ for AOML-ET in default configuration with the average global 23-year trend of $-0.173 \text{ mol m}^{-2} \text{ decade}^{-1}$ removed. (b) *P*-values for the trends. The large positive and negative trends in (a) have *P*-values of less than 0.01 that are statistically significant. (c) Map of trends using $\Delta f\text{CO}_2$ rather than the default $f\text{CO}_{2w}$ as the target with the average global 23-year trend of $-0.105 \text{ mol m}^{-2} \text{ decade}^{-1}$ removed.

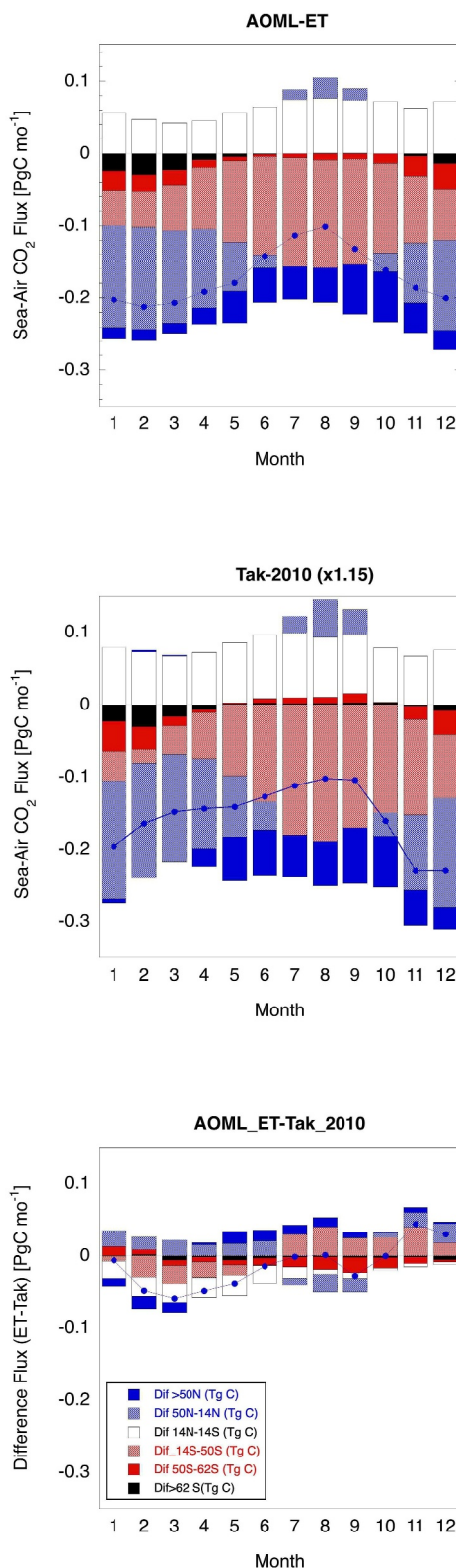


Figure 8. Regional monthly zonal sea-air CO_2 fluxes based on the (a) AOML-ET; (b) Tak-2010, scaled to the same surface area (x1.15); and (c) the difference. The different zones following Takahashi et al. (2009) are listed in the legend. The lines with blue circles represent the global monthly fluxes for 2010. Fluxes are expressed in PgC month^{-1} .

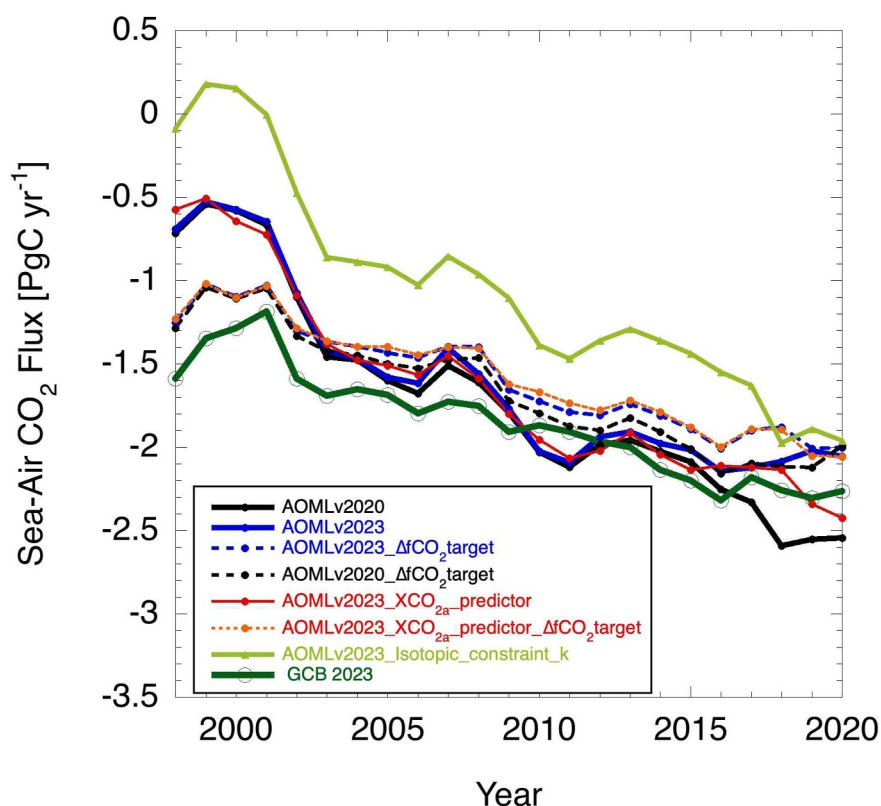


Figure 9. Global net sea-air CO₂ fluxes from 1998 to 2020 using $f\text{CO}_{2w}$ and $\Delta f\text{CO}_2$ as target variables for the AOML-ET method. Solid black line: default AOML-ETv2020; solid blue line: AOML-ETv2023; dashed black line: AOML-ETv2020 with $\Delta f\text{CO}_2$ as target; dashed blue line: AOML-ETv2023 with $\Delta f\text{CO}_2$ as target; solid red line: AOML-ETv2023 with XCO_{2a} as predictor; and dashed orange line: AOML-ETv2023 with XCO_{2a} as predictor and $\Delta f\text{CO}_2$ as the target; green line: AOML-ETv2020 with k based on the isotopic constraint (Equation 6). The statistical analysis of the linear regressions to the different runs is given in Table S2 in Supporting Information S1.

the two methods yield similar global and regional results, consistent with previous findings that different gap-filling methods do not significantly affect flux patterns (Gregor et al., 2019).

3.3. Sensitivity of Fluxes to $\Delta f\text{CO}_2$

Using $\Delta f\text{CO}_2$ as a target variable shows a large decrease in CO₂ uptake compared to the default configuration using $f\text{CO}_{2w}$ as a target. When using $\Delta f\text{CO}_2$ as a target, the $\Delta f\text{CO}_2$, which is the thermodynamic forcing variable in the bulk flux formulation (Equation 2), is mapped rather than the $f\text{CO}_{2w}$. This small procedural difference results in substantial changes in the magnitude and trends of the fluxes. The global sea-air CO₂ fluxes are -1.3 PgC yr^{-1} in 1998 and -2.0 PgC yr^{-1} in 2020 when using $\Delta f\text{CO}_2$ as a target. In contrast, the default AOML-ETv2020 fluxes are -0.7 PgC yr^{-1} for 1998 and -2.5 PgC yr^{-1} for 2020 (Figure 9). Correspondingly, the trend for the $\Delta f\text{CO}_2$ target run is $-0.51 \text{ PgC yr}^{-1} \text{ decade}^{-1}$, compared to $-0.89 \text{ PgC yr}^{-1} \text{ decade}^{-1}$ for the default AOML-ETv2020 from 1998 to 2020 (Table 1). Having $\Delta f\text{CO}_2$ instead of $f\text{CO}_{2w}$ as the target variable shows slightly better overall agreement with test data. The Taylor diagram (Figure 6) shows an RMSE of $18 \mu\text{atm}$, a standard deviation of $37 \mu\text{atm}$, and an r^2 of 0.88.

The decadal trend using $\Delta f\text{CO}_2$ as the target variable aligns with the consensus value used in the Global Carbon Budget, GCB-2023 (Friedlingstein et al., 2023) based on an ensemble average of observation-based and global ocean biogeochemical model results. The annual ocean CO₂ uptake values of GCB-2023 are shown in Figures 1 and 9. The higher uptake at the beginning of the record and lower uptake at the end compared to many of the observation-based estimates that map $f\text{CO}_{2w}$ is apparent. AOML-ET with $\Delta f\text{CO}_2$ as a target shows good correspondence with the sea-air CO₂ flux trend of the GCB-2023 values but with an average of 0.2 PgC yr^{-1} less uptake. In RECCAP2, the oceanic anthropogenic carbon uptake is estimated from the output of an ocean

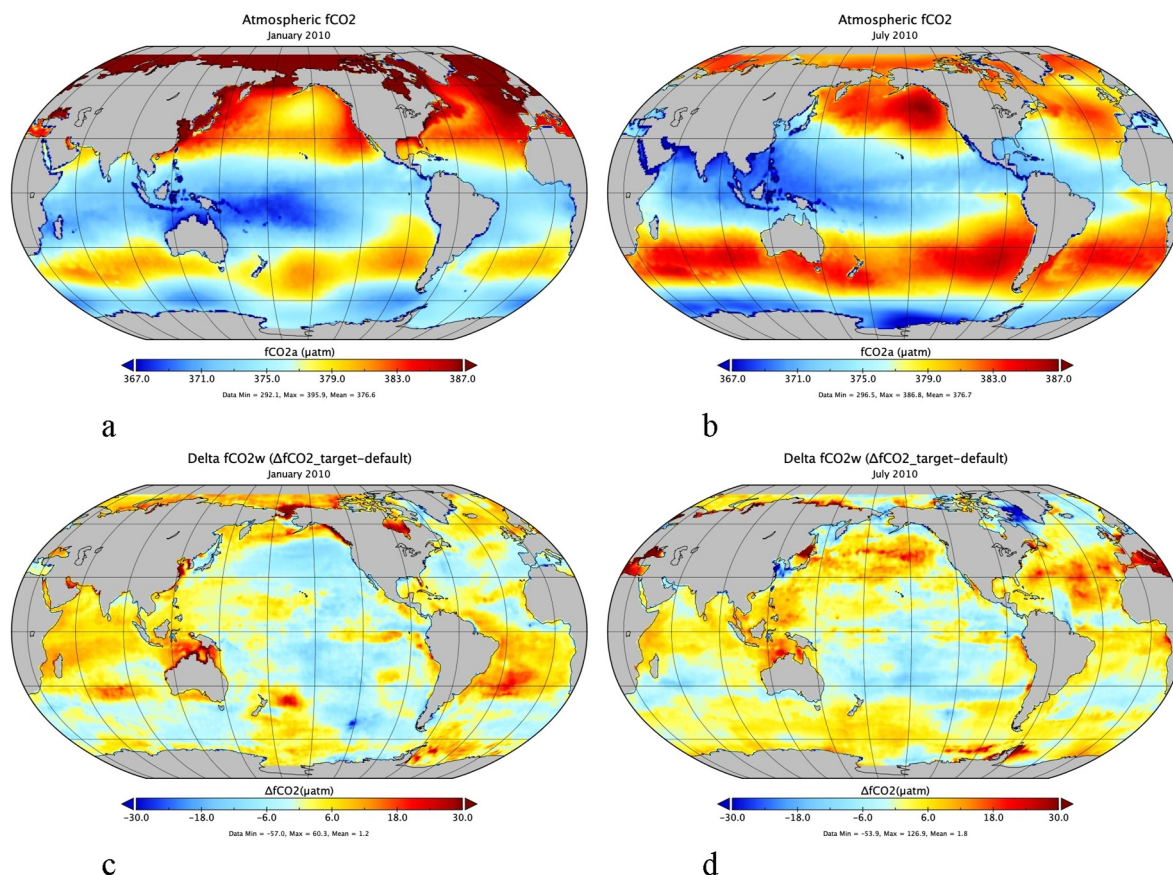


Figure 10. (a) $f\text{CO}_{2a}$ for January 2010; (b) $f\text{CO}_{2a}$ for July 2010; (c) Difference in $\Delta f\text{CO}_2$ between using $\Delta f\text{CO}_2$ and $f\text{CO}_{2w}$ as a target for January 2010 for AOML-ETv2020; (d) Same as (c) but for July 2010. Areas in blue show a greater positive or smaller negative $\Delta f\text{CO}_2$ in the default configuration and thus greater effluxes or smaller influxes.

circulation inverse model (OCIM) with a decadal trend of $-0.41 \pm 0.03 \text{ PgC yr}^{-1} \text{ decade}^{-1}$ for 2001–2018 (de Vries et al., 2023). The larger negative trend of the observation-based products is attributed to a climate trend. As noted in de Vries et al. (2023), “This putative climate-forced strengthening of the ocean carbon sink since 2001 in the $p\text{CO}_2$ products is not apparent in the GOBMs, and thus the robustness of and the reasons for this trend remain unclear.” The results with AOML-ET using $f\text{CO}_2$ as the target variable suggest that this may be an artifact of the methodology.

The large differences in global sea-air CO_2 fluxes and the lower trend when using $\Delta f\text{CO}_2$ as a target, as opposed to $f\text{CO}_{2w}$, are due to subtle regional and seasonal differences between $\Delta f\text{CO}_2$ and $\Delta f\text{CO}_2$ calculated from separate $f\text{CO}_{2w}$ and $f\text{CO}_{2a}$ fields. The spatial patterns of $f\text{CO}_{2w}$ and $\Delta f\text{CO}_2$ differ due to seasonal variations in $f\text{CO}_{2a}$ (Figure 10). $f\text{CO}_{2a}$ is determined from $X\text{CO}_{2a}$, which shows higher values in winter and lower values in summer, with an amplitude of 8 ppm in the Northern Hemisphere. However, SST and pressure (P) also affect $f\text{CO}_{2a}$. High temperatures and associated high water vapor content lead to lower $f\text{CO}_{2a}$ values in tropical regions, whereas lower barometric pressures in Equatorial and Southern high-latitude regions depress $f\text{CO}_{2a}$ (Figures 10a and 10b). These differences in $f\text{CO}_{2a}$ influence the training of the model when $\Delta f\text{CO}_2$ is used as a target. The resulting impact on regional trends is mapped in Figure 7c. In high-latitude regions, where there is a negative trend compared to the mean sea-air CO_2 flux trend, the use of $\Delta f\text{CO}_2$ as a target results in a smaller influx (Figures 7a–7c). In tropical and subtropical regions, the trends are positive, but the positive trend is less pronounced, leading to a smaller influx over time when $\Delta f\text{CO}_2$ is the target.

The global average $f\text{CO}_{2w}$ difference between using $f\text{CO}_{2w}$ and $\Delta f\text{CO}_2$ as targets shows lower $f\text{CO}_{2w}$ at the start of the record and higher at the end (Figure 11). This pattern is consistent with the different trends in flux. The seasonal progression of fluxes using the two different targets is similar and only differs in magnitude. The

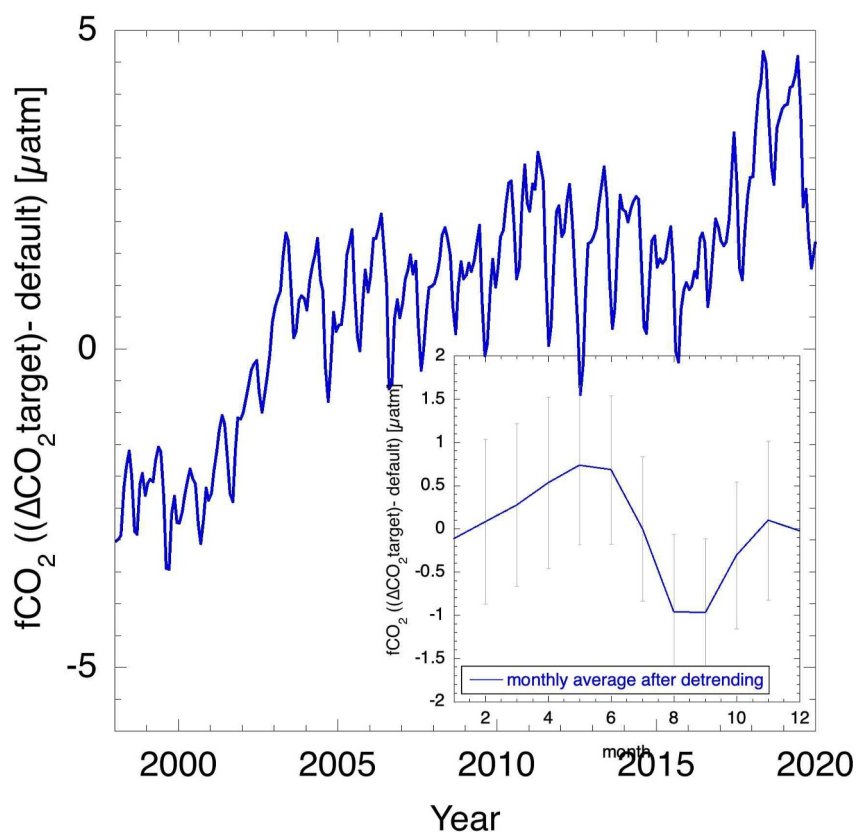


Figure 11. Difference in global average $f\text{CO}_{2w}$ between using $\Delta f\text{CO}_2$ and $f\text{CO}_{2w}$ as targets versus time in μatm . The inset shows the monthly average difference obtained by subtracting the 20-year trend.

minimum in differences is in August-September, which is the period of the smallest global $\Delta f\text{CO}_2$ disequilibrium, and a maximum difference is in May-June (inset, Figure 11). This leads to greater seasonal amplitude in sea-air CO_2 fluxes for $\Delta f\text{CO}_2$ as the target. The monthly fluxes for 2010 are shown in Figure 12, with a minimum in fluxes (greatest uptake) in the boreal winter months (Jan-March) and a maximum in summer (August).

Comparison of feature importance of the predictor variables (Figure 13) between using $f\text{CO}_{2w}$ and $\Delta f\text{CO}_2$ as targets shows a similar dependency on predictors except for time (JDN), which has greater importance for $f\text{CO}_{2w}$ with a score of 0.13 versus 0.05 for $\Delta f\text{CO}_2$. Other scores are similar with location, expressed as the sum of latitude (LAT) and vector longitudes, sine (SLON) and cosine (CLON), being the strongest predictor with a cumulative score of 0.33 for the $f\text{CO}_{2w}$ scenario and 0.37 for $\Delta f\text{CO}_2$. This is followed by SST with a score of 0.21 for $f\text{CO}_{2w}$ and 0.25 for $\Delta f\text{CO}_2$. The strong dependence of $f\text{CO}_{2w}$ and $\Delta f\text{CO}_2$ with SST is similar to most other gap-filling techniques (Bennington et al., 2022) due to the strong physical and chemical dependency of $f\text{CO}_{2w}$ with temperature of $\partial f\text{CO}_{2w} / \partial T^{-1} = 0.042$ (Wanninkhof et al., 2022). Time, expressed as month since October 1997, is the main predictor of trends as atmospheric CO_2 levels increase with time. While some gap-filling approaches, notably MLR interpolations, have shown weak correlation with Chl-a, Chl-a is significant in the construction of the AOML-ET with a score of 0.1. The other predictor variables, MLD and SSS, have similar scores of ≈ 0.1 .

3.4. Sensitivity of Sea-Air CO_2 fluxes to Atmospheric Forcing by XCO_{2a}

The impact of atmospheric forcing by XCO_{2a} is examined by replacing time (JDN expressed as month since October 1997) with annual averaged XCO_{2a} values, as is done in Landschützer et al. (2016). JDN increases monotonically, while XCO_{2a} varies year to year, with growth rates increasing from about 1.5 ppm yr^{-1} to 2.5 ppm yr^{-1} over the period from 1998 to 2022 (https://gml.noaa.gov/ccgg/trends/gl_gr.html, accessed 5/9/2024). Using XCO_{2a} as a predictor results in little difference in global fluxes up to 2019, after which the run with

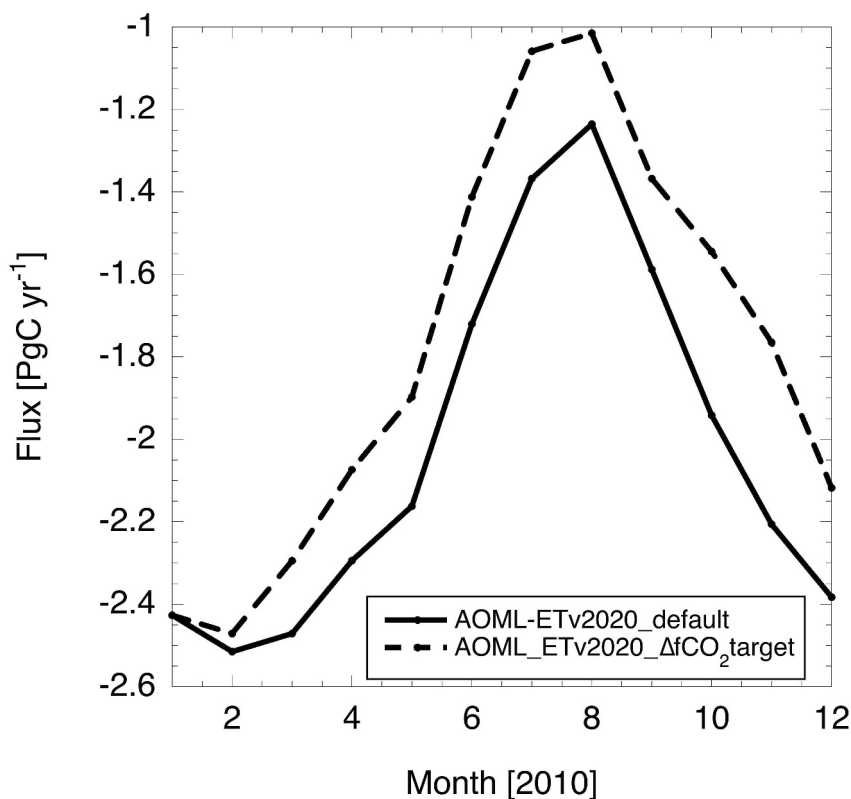


Figure 12. Monthly fluxes using $f\text{CO}_{2w}$ as the target variable in AOML-ET for 2010 (solid line) and using $\Delta f\text{CO}_2$ as the target variable in AOML-ET for 2010 (dashed line).

$X\text{CO}_{2a}$ shows about 0.4 PgC yr^{-1} greater uptake, attributed to rapidly increasing $X\text{CO}_{2a}$ and possibly tail effects toward the end of the record (Figure S6 in Supporting Information S1).

In the default configuration of AOML-ET, a zonally homogeneous $X\text{CO}_{2a}$ product, MBL-RS, is applied since the lower troposphere mixes zonally on the order of a month. However, small deviations in $X\text{CO}_{2a}$ can have a large impact on sea-air CO_2 fluxes. For example, a 1 ppm offset in $X\text{CO}_{2a}$ causes a bias in $\Delta f\text{CO}_2$ of about $1 \mu\text{atm}$ and changes the global sea-air CO_2 flux by $\approx 0.2 \text{ PgC yr}^{-1}$. Of note is that the zonal homogeneity in $X\text{CO}_{2a}$ of the MBL-RS product is not reflected in $f\text{CO}_{2a}$ due to regional differences in barometric pressure (P) and saturation water vapor pressure ($p\text{H}_2\text{O}$) (Equation 4). These can cause zonal differences of up to $\approx 16 \mu\text{atm}$ in $f\text{CO}_{2a}$ even with constant $X\text{CO}_{2a}$ (Figures 10a and 10b). However, P and $p\text{H}_2\text{O}$ both affect the $f\text{CO}_{2w}$ and $f\text{CO}_{2a}$ in a similar fashion, such that small errors in P and $p\text{H}_2\text{O}$ will not have a large impact on $\Delta f\text{CO}_2$ if the same P and SST products are used to calculate both $f\text{CO}_{2w}$ and $f\text{CO}_{2a}$.

Deviations from near-constant zonal $X\text{CO}_{2a}$ levels in the MBL occur when air flows off continents that generally contain higher CO_2 due to fossil fuel burning and net ecosystem respiration on land during the fall and winter months. This leads to higher $X\text{CO}_{2a}$ over many coastal seas and larger influxes/lower effluxes, particularly along the heavily industrialized eastern continental boundaries in the Northern Hemisphere due to the prevailing westerly winds at those latitudes (Wanninkhof et al., 2019). However, during spring and summer, carbon uptake on land due to terrestrial photosynthesis can lead to negative zonal anomalies in $X\text{CO}_{2a}$ downwind from land in coastal regions, which leads to decreased ocean CO_2 uptake, but these anomalies are significantly smaller. Northcott et al. (2019) suggested from bold extrapolation of nearshore observations that the higher PBL $X\text{CO}_2$ could enhance global ocean CO_2 uptake by 1%.

Quantitatively, the impact of higher $X\text{CO}_{2a}$ in coastal regions is assessed by comparing the spatially resolved CT-PBL product with the zonally averaged MBL-RS product. The difference in global fluxes between the CT-PBL product and the MBL-RS product is small, as the $X\text{CO}_{2a}$ of both products is constrained by the same MBL observations. The average difference in global monthly ocean sink between the CT-PBL and the MBL-RS $X\text{CO}_{2a}$

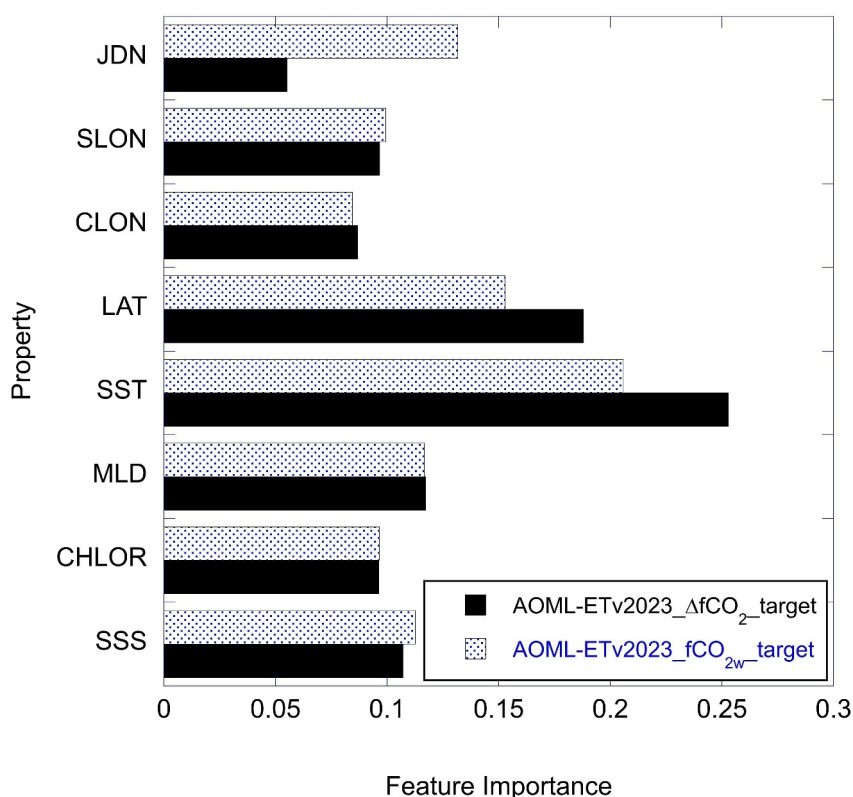


Figure 13. Importance of the different predictor variables using AOML-ET with $f\text{CO}_{2w}$ (stippled bars) and $\Delta f\text{CO}_2$ (black bars) as target variables. Location (latitude (Lat) and longitude (SLON and CLON)) has the greatest importance, followed by SST. Month since Oct 1997 (JDN) has a smaller significance when using $\Delta f\text{CO}_2$ as a target. Mixed layer depth (MLD), sea surface salinity (SSS), and Chl-a (CHLOR) have similar importance.

is $-0.02 \pm 0.05 \text{ PgC yr}^{-1}$ from 2000 to 2020, with the CT-PBL product showing slightly greater fluxes ($\approx 1\%$) into the ocean on average, in accordance with the estimate of Northcott et al. (2019). No appreciable year-to-year differences are observed. However, regional differences in sea-air CO_2 fluxes can be large, especially in the winter months. The largest increases in influxes using the CT-PBL product are off the East Coasts of North America and Asia. Figure 14 shows the differences in the 30–35°N latitude band for 2010 between fluxes derived from the MBL-RS and CT-PBL. The entire latitude band shows the characteristic seasonal pattern for the subtropical oceans, with a strong sink in winter and a weak source in summer. The annual average flux density for 2010 was $-0.61 \text{ mol m}^{-2} \text{ yr}^{-1}$ for the MBL-RS product and $-0.66 \text{ mol m}^{-2} \text{ yr}^{-1}$ for the CT-PBL product. The Mid-Atlantic Bight (MAB) off the coast of the USA (30°N–35°N, 75°W–70°W) and the Yellow Sea (30°N–35°N, 120°W–125°W) show wintertime enhancement of uptake by 6% and 21%, respectively. Differences in fluxes between the two MBL products in spring and summer are smaller, with the MAB showing a slightly decreased influx during May for the CT-PBL product attributed to XCO_{2a} drawdown on land due to the springtime increase in terrestrial biological productivity.

The results agree with a similar exercise performed by Palter et al. (2023), who used a zonal mean of CT-PBL XCO_{2a} rather than the MBL-RS XCO_{2a} product. They also used the SOM-FFN ML approach of Jersild and Landschützer (2024) to recreate the $p\text{CO}_{2w}$ fields. This suggests that using different MBL XCO_{2a} products will likely lead to quantitatively similar estimates for sea-air CO_2 fluxes derived for all ML and interpolation approaches.

3.5. Sensitivity to the Gas Transfer Velocity

Different gas transfer velocity formulations and wind speed products can significantly affect global flux estimates, with recent studies suggesting that gas transfer is a primary source of uncertainty in the sea-air CO_2 flux estimates (Ford et al., 2024; Jersild & Landschützer, 2024; Woolf et al., 2019). Several aspects of the effect of gas

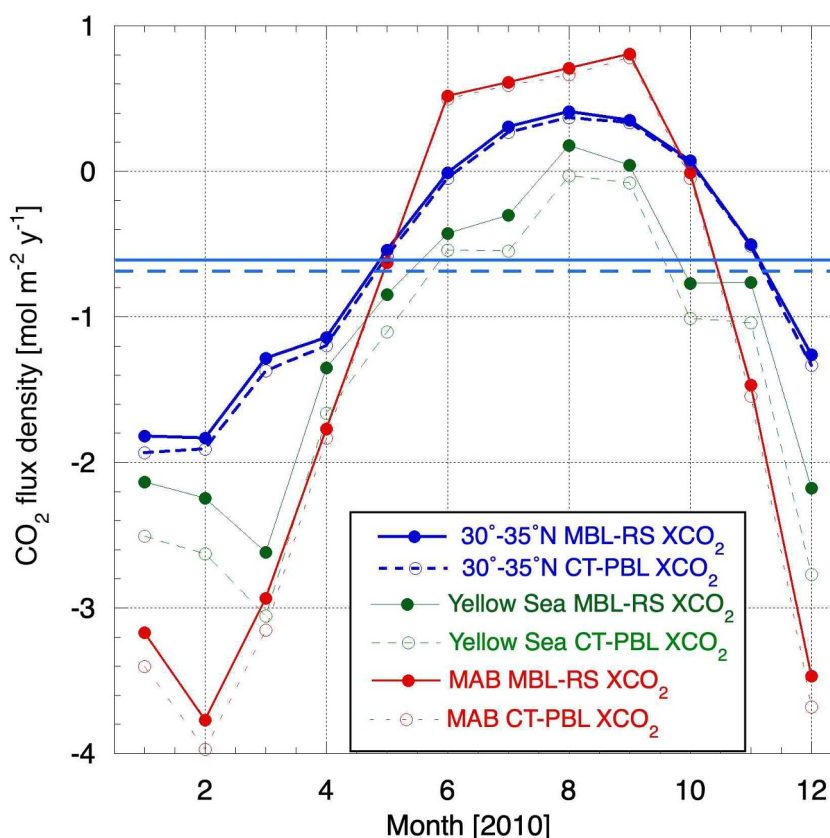


Figure 14. Monthly averaged sea-air CO_2 flux densities in the $30^\circ\text{--}35^\circ\text{N}$ latitude band using different XCO_{2a} products and the AOML-ETv2020 for $f\text{CO}_{2w}$ values. The MBL XCO_{2a} product (solid line; solid circles) and PBL XCO_{2a} product (dashed lines; open circles) are shown versus month for 2010. The thin blue lines are the monthly zonally averaged flux densities for $30^\circ\text{--}35^\circ\text{N}$; the green lines are monthly flux densities over the Yellow Sea ($30^\circ\text{--}35^\circ\text{N}$); the red lines are the monthly flux densities over the Mid-Atlantic Bight ($30^\circ\text{--}35^\circ\text{N}$). The horizontal solid and dashed blue lines represent the annual average fluxes using the MBL and PBL products, respectively, in the $30^\circ\text{--}35^\circ\text{N}$ latitude band.

transfer on fluxes, such as the impact of time averaging and different wind fields, have been investigated (Gregor et al., 2019; Roobaert et al., 2018; Wanninkhof et al., 2002). However, conical quadratic wind speed relationships are commonly used to parameterize gas transfer in most observation-based flux estimates, including those in RECCAP2 (de Vries et al., 2023) and the GCB (Friedlingstein et al., 2023). The functional form of the parameterizations is of increasing importance with improved high-resolution wind speeds and $\Delta f\text{CO}_2$ -mapped products that better capture extremes and variability, such that the variability of $\langle u^2 \rangle$ and $\Delta f\text{CO}_2$ are better represented. The three gas exchange wind parameterizations compared here are constrained with the global ocean bomb ^{14}C inventories. In the case of the parameterization inferred from Krakauer et al. (2006), it uses ^{13}C constraints as well. This relationship is referred to as the isotopic constraint.

The default parameterization is depicted in Equation 3; the polynomial expression referred to as a hybrid dependency is shown in Equation 5; and the weak wind speed dependence of the isotopic constraint is provided in Equation 6. They are displayed graphically in Figure 2. Most laboratory and field studies (Butterworth & Miller, 2016; Ho et al., 2011; Yang et al., 2022) suggest that the results can be well represented by quadratic or polynomial wind speed dependencies. However, uncertainties remain about the magnitude of fluxes at low and high wind speeds and the mechanisms driving these fluxes. Thus, the isotopic constraint can be considered an endmember scenario, where direct wind effects play a lesser role and other factors affecting surface turbulence and gas transfer become more prominent.

The quadratic and hybrid dependencies show negligible differences in annual global sea-air CO_2 flux of $0.003 \pm 0.011 \text{ PgC yr}^{-1}$ from 1998 to 2020. While the global results are similar, regional flux patterns differ

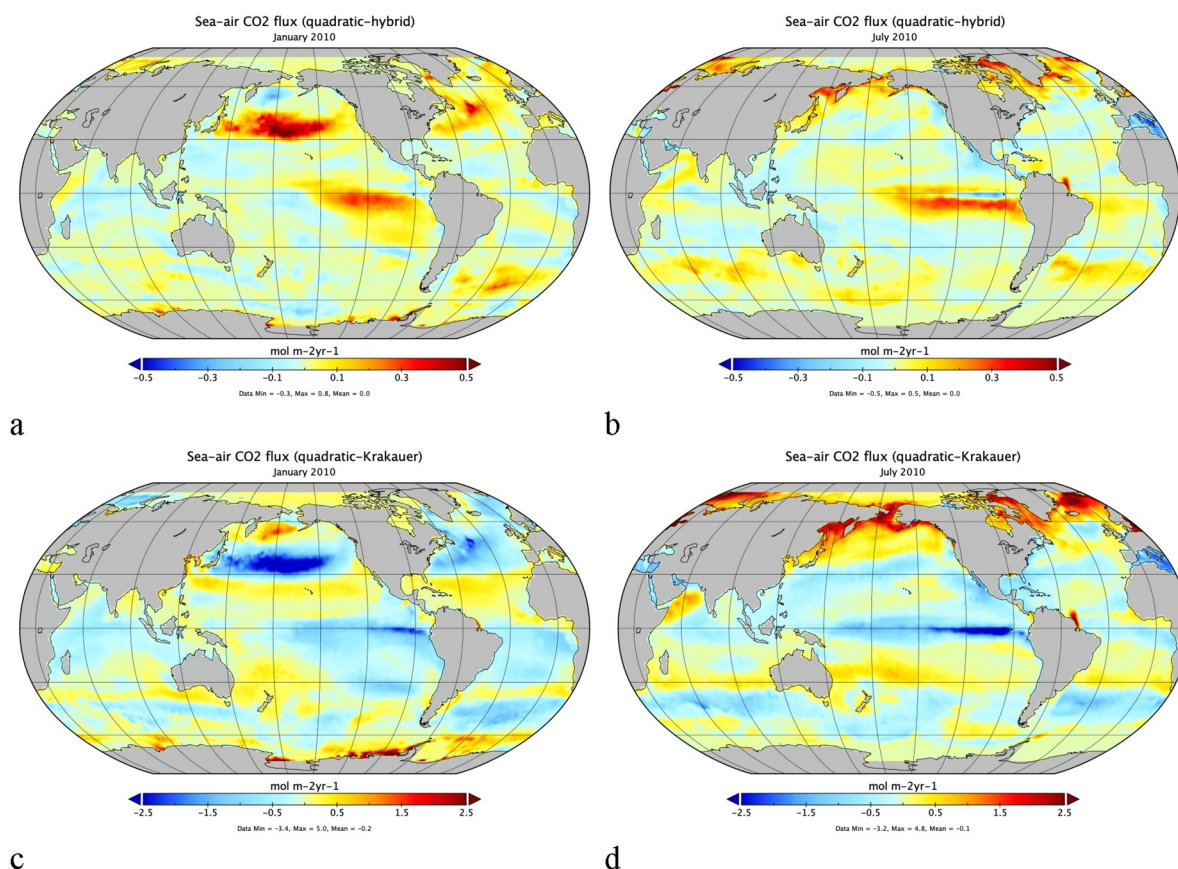


Figure 15. Maps of differences in sea-air CO₂ flux densities between the square wind speed and hybrid relationships for gas transfer for January (a) and July (b) 2010; and between the square wind speed and Krakauer-isotopic constraint for January (c) and July (d) 2010 using AOML-ET. The flux densities for January and July 2010 using AOML-ET and the default wind speed squared relationship are shown in Figure 5. Color bars have units of mol m⁻² yr⁻¹.

significantly. Figures 15a and 15b show maps of flux differences between the quadratic and hybrid relationships for January and July 2010, respectively. The relationships of k versus $\langle u \rangle$ cross at 5.9 m s⁻¹ and 13 m s⁻¹, with the hybrid relationship showing slightly lower k between the two crossovers. Most of the windspeeds over the global ocean are in this range (Figure 2, inset). At low and high winds, the hybrid parameterization yields higher k values (Figure 2). As a result, the hybrid expression shows larger fluxes in regions with low winds that are persistently less than 5 m s⁻¹. These include the tropical and sub-tropical regions of the ocean during the summer season for the respective hemispheres depicted by light blue shading in Figures 15a and 15b. A notable exception is in the Eastern Equatorial Pacific south of the Equator, showing higher effluxes with the quadratic expression because winds there average 6–7 m s⁻¹. Only a few extratropical regions show larger fluxes with the hybrid expression, which are areas with persistent high winds of greater than 13 m s⁻¹. The southern area of the Bering Sea in January 2010 showed higher fluxes with the hybrid parameterization, and since this region has positive $\Delta f\text{CO}_2$, it leads to higher effluxes (Figure 15a). During July, the winds are less on average 13 m s⁻¹ in this region, and correspondingly, a quadratic expression leads to higher effluxes (Figure 15b). The mid-latitude regions with prevailing winds between 5 and 13 m s⁻¹ will have lower k with a hybrid parameterization and correspondingly show lower fluxes.

The crossover point between the quadratic and isotopic dependency occurs at 9 m s⁻¹ (Figure 2), with the quadratic showing lower k below this wind speed and higher k above. The impact on the flux density distribution is significant as 75% of global winds are below 9 m s⁻¹ (Figure 2, inset). Using k obtained from the isotopic constraint yields an influx that is on average 0.61 ± 0.04 PgC yr⁻¹ less than the default quadratic (Figure 9). However, the 23-year global annual trends in the fluxes using AOML_ETv2020 are the same at 0.089 PgC yr⁻¹ decade⁻¹ between the k parameterized as a quadratic with wind speed or with the isotopic constraint.

As shown in Wanninkhof et al. (2009), the global distribution of flux densities predominantly shows effluxes at low wind speeds and influxes at higher winds. Thus, a dependence of k versus u_{10} that is stronger at low winds and less at high winds, such as that of the isotopic constraint, results in smaller effluxes and influxes, both of which contribute to a smaller global CO_2 uptake. Figures 15c and 15d show differences between the isotopic and the quadratic dependencies for January 2010 and July 2010, with the color scale range five times greater than Figures 15a and 15b. Much smaller influxes are observed with the isotopic constraint in the North Pacific (30°N – 45°N) for January 2010, where mean winds are greater than 9 m s^{-1} (Figure 15c). Further north there is a region of outgassing (Figure 5a) with winds greater than 9 m s^{-1} showing the depressed outgassing with the isotopic constraint. South of 30°S the region is a weak sink with the isotopic constraint yielding greater influxes. The equatorial areas are regions of outgassing with winds less than 9 m s^{-1} , and the isotopic constraint shows greater effluxes. For July 2010, the northern high-latitude sink regions ($>60^\circ\text{N}$) in summertime show a greater influx of over $2.5\text{ mol m}^{-2}\text{ yr}^{-1}$ with the isotopic constraint compared to the quadratic through a combination of average wind being less than 9 m s^{-1} and large negative ΔfCO_2 . The strong positive anomaly in the difference in the Amazon outflow region (equator, 50°W) is due to large negative ΔfCO_2 and low winds causing more uptake with the method involving the isotopic constraint.

4. Conclusions

The machine learning (ML) approach AOML-ETv2020 shows an average global sea-air CO_2 flux of -1.70 PgC yr^{-1} from 1998 to 2020. This value aligns with other ML approaches but exhibits a 30% greater long-term trend of $-0.89\text{ PgC yr}^{-1}\text{ decade}^{-1}$, compared to the average trend of other ML and interpolation methods used in the recent RECCAP-2 reanalysis. This stronger trend is largely attributed to low fluxes at the beginning of the time series caused, in part, by a training period that started in 1998. The spatial patterns and magnitude of regional fluxes from AOML-ETv2020 are similar to those in the updated Takahashi climatology for 2010. These results confirm previous findings that suggest that the spatial gap filling approach for $\text{fCO}_{2\text{w}}$ does not significantly affect global sea-air CO_2 flux estimates, provided there is sufficient observational coverage of both target and predictor variables.

However, sea-air CO_2 fluxes are sensitive to atmospheric forcing, particularly through gas transfer, $\text{XCO}_{2\text{a}}$, and ΔfCO_2 . Notably, when using ΔfCO_2 as a target instead of $\text{fCO}_{2\text{w}}$ in AOML-ET, the 23-year average uptake remains similar at -1.65 PgC yr^{-1} but with a much weaker negative trend of $-0.51\text{ PgC yr}^{-1}\text{ decade}^{-1}$. This trend agrees with the consensus estimate provided in the Global Carbon Budget and with the results of an ocean inverse model. Better-resolved marine boundary layer (MBL) $\text{XCO}_{2\text{a}}$ values reveal large regional differences in fluxes, especially in continental outflow regions. Different parameterizations of gas transfer velocities with wind speed lead to substantial regional differences in fluxes, although global effects remain small. An exception is relationships with weak wind speed dependencies, which show significantly less global CO_2 uptake despite being constrained by the same global bomb ^{14}C inventory.

The results show that atmospheric forcing has a determining factor on sea-air CO_2 fluxes. Improved forcing fields should be implemented in future assessments of oceanic CO_2 uptake. Temporally and spatially resolved $\text{XCO}_{2\text{a}}$ products are recommended for atmospheric forcing to better capture sea-air CO_2 fluxes, particularly in the coastal realm. Applying machine learning approaches to ΔfCO_2 rather than $\text{fCO}_{2\text{w}}$ as a target will avoid mismatches in air and water values and possible bias in results. Investigating if all machine learning approaches show similar sensitivity to choice of target should be investigated.

Data Availability Statement

The AOML-ET results (1998–2018) and Takahashi 2010 climatology based on $\text{fCO}_{2\text{w}}$ data from 1985 to 2018 can be found as part of the RECCAP2 holdings at Müller, J.D. (2023): <https://doi.org/10.5281/zenodo.7990823>, Zenodo. The SOCATv2020 gridded data is obtained from <https://doi.org/10.25921/4xkx-ss49> (Bakker et al., 2020). SOCATv2023 is from <https://doi.org/10.25921/r7xa-bt92> (Bakker et al., 2023). The outputs of AOML-ETv2020 and v2023, and predictor variables used can be found under NCEI Accession 0298989: <https://www.ncei.noaa.gov/data/oceans/ncei/ocads/metadata/0298989.html> (Wanninkhof et al., 2024).

- Jacobson, A. R., Schuldt, K. N., Miller, J. B., Oda, T., Tans, P., Andrews, A., et al. (2020). *CarbonTracker CT2019B*. NOAA Global Monitoring Laboratory. <https://doi.org/10.25925/20201008>
- Jersild, A., & Landschützer, P. (2024). A spatially explicit uncertainty analysis of the air-sea CO₂ flux from observations. *Geophysical Research Letters*, 51(4), e2023GL106636. <https://doi.org/10.1029/2023GL106636>
- Krakauer, N. Y., Randerson, J. T., Primau, F. W., Gruber, N., & Menemenlis, D. (2006). Carbon isotope evidence for the latitudinal distribution and wind speed dependence of the air-sea gas transfer velocity. *Tellus B: Chemical and Physical Meteorology*, 58(5), 390–417. <https://doi.org/10.1111/j.1600-0889.2006.00223.x>
- Krol, M., Houweling, S., Bregman, B., van den Broek, M., Segers, A., van Velthoven, P., et al. (2005). The two-way nested global chemistry-transport zoom model TM5: Algorithm and applications. *Atmospheric Chemistry and Physics*, 5(2), 417–432. <https://doi.org/10.5194/acp-5-417-2005>
- Landschützer, P., Gruber, N., & Bakker, D. C. E. (2016). Decadal variations and trends of the global ocean carbon sink. *Global Biogeochemical Cycles*, 30(10), 1396–1417. <https://doi.org/10.1002/2015GB005359>
- Landschützer, P., Gruber, N., Bakker, D. C. E., Schuster, U., Nakaoka, S., Payne, M. R., et al. (2013). A neural network-based estimate of the seasonal to inter-annual variability of the Atlantic Ocean carbon sink. *Biogeosciences*, 10(11), 7793–7815. <https://doi.org/10.5194/bg-10-7793-2013>
- Landschützer, P., Gruber, N., Bakker, D. C. E., Stemmler, I., & Six, K. D. (2018). Strengthening seasonal marine CO₂ variations due to increasing atmospheric CO₂. *Nature Climate Change*, 8(2), 146–150. <https://doi.org/10.1038/s41558-017-0057-x>
- Lee, K., Wanninkhof, R., Takahashi, T., Doney, S., & Feely, R. A. (1998). Low interannual variability in recent oceanic uptake of atmospheric carbon dioxide. *Nature*, 396(6707), 155–159. <https://doi.org/10.1038/24139>
- Li, Z., Adamec, D., Takahashi, T., & Sutherland, S. C. (2005). Global autocorrelation scales of the partial pressure of oceanic CO₂. *Journal of Geophysical Research*, 110(C8), C08002. <https://doi.org/10.1029/2004JC002723>
- Liu, W., & Xie, S.-P. (2018). An Ocean view of the global surface warming hiatus. *Oceanography*, 31(2). <https://doi.org/10.5670/oceanog.2018.217>
- Magnan, A. K., Colombier, M., Bille, R., Joos, F., Hoegh-Guldberg, O., Portner, H.-O., et al. (2016). Implications of the Paris agreement for the ocean. *Nature Climate Change*, 6(8), 732–735. <https://doi.org/10.1038/nclimate3038>
- McKinley, G. A., Fay, A. R., Edebbbar, Y. A., Gloege, L., & Lovenduski, N. S. (2020). External forcing explains recent decadal variability of the ocean carbon sink. *AGU Advances*, 1(2), e2019AV000149. <https://doi.org/10.1029/2019AV000149>
- Müller, J. D. (2023). *RECCAP2-ocean data collection [Version V1]*. Zenodo. <https://doi.org/10.5281/zenodo.7990823>
- Northcott, D., Sevadjian, J., Sancho-Gallegos, D. A., Wahl, C., Friederich, J., & Chavez, F. P. (2019). Impacts of urban carbon dioxide emissions on sea-air flux and ocean acidification in nearshore waters. *PLoS One*, 14(3), e0214403. <https://doi.org/10.1371/journal.pone.0214403>
- Palter, J. B., Nickford, S., & Mu, L. (2023). Ocean carbon dioxide uptake in the tailpipe of industrialized continents. *Geophysical Research Letters*, 50(21), e2023GL104822. <https://doi.org/10.1029/2023GL104822>
- Park, G.-H., Wanninkhof, R., Doney, S. C., Takahashi, T., Lee, K., Feely, R. A., et al. (2010). Variability of global net sea-air CO₂ fluxes over the last three decades using empirical relationships. *Tellus*, 62B(5), 352–368. <https://doi.org/10.1111/j.1600-0889.2010.00498.x>
- Pierrot, D., Neil, C., Sullivan, K., Castle, R., Wanninkhof, R., Lueger, H., et al. (2009). Recommendations for autonomous underway pCO₂ measuring systems and data reduction routines. *Deep-Sea Res II*, 56, 512–522.
- Rödenbeck, C., Bakker, D. C. E., Gruber, N., Iida, Y., Jacobson, A. R., Jones, S., et al. (2015). Data-based estimates of the ocean carbon sink variability—first results of the Surface Ocean pCO₂ Mapping intercomparison (SOCOM). *Biogeosciences*, 12(23), 7251–7278. <https://doi.org/10.5194/bg-12-7251-2015>
- Rödenbeck, C., deVries, T., Hauck, J., Le Quéré, C., & Keeling, R. F. (2022). Data-based estimates of interannual sea-air CO₂ flux variations 1957–2020 and their relation to environmental drivers. *Biogeosciences*, 19(10), 2627–2652. <https://doi.org/10.5194/bg-19-2627-2022>
- Roobaert, A., Laruelle, G. G., Landschützer, P., & Regnier, P. (2018). Uncertainty in the global oceanic CO₂ uptake induced by wind forcing: Quantification and spatial analysis. *Biogeosciences*, 15(6), 1701–1720. <https://doi.org/10.5194/bg-15-1701-2018>
- Roobaert, A., Regnier, P., Landschützer, P., & Laruelle, G. G. (2023). A novel sea surface pCO₂-product for the global coastal ocean resolving trends over the 1982–2020 period. *Earth System Science Data Discussions*, 2023, 1–32. <https://essd.copernicus.org/preprints/essd-2023-228/>
- Sharp, J. D., Fassbender, A. J., Carter, B. R., Lavin, P. D., & Sutton, A. J. (2022). A monthly surface pCO₂ product for the California Current Large Marine Ecosystem. *Earth System Science Data*, 14(4), 2081–2108. <https://doi.org/10.5194/essd-14-2081-2022>
- Stamell, J., Rustagi, R. R., Gloege, L., & McKinley, G. A. (2020). Strengths and weaknesses of three Machine Learning methods for pCO₂ interpolation. *Geoscientific Model Development Discussions*, 2020, 1–25. <https://gmd.copernicus.org/preprints/gmd-2020-311/>
- Sweeney, C., Gloor, E., Jacobson, A. R., Key, R. M., McKinley, G., Sarmiento, J. L., & Wanninkhof, R. (2007). Constraining global air-sea gas exchange for CO₂ with recent bomb C-14 measurements. *Global Biogeochemical Cycles*, 21(2), GB2015. <https://doi.org/10.1029/2006gb002784>
- Takahashi, T., Feely, R. A., Weiss, R., Wanninkhof, R., Chipman, D. W., Sutherland, S. C., & Takahashi, T. T. (1997). Global air-sea flux of CO₂: An estimate based on measurements of sea-air pCO₂ difference. *Proceedings of the National Academy of Sciences of the United States of America*, 94(16), 8292–8299. <https://doi.org/10.1073/pnas.94.16.8292>
- Takahashi, T., Sutherland, S. C., Wanninkhof, R., Sweeney, C., Feely, R. A., Chipman, D. W., et al. (2009). Climatological mean and decadal change in surface ocean pCO₂ and net sea-air CO₂ flux over the global oceans. *Deep-Sea Res II*, 2009(8–10), 554–577. <https://doi.org/10.1016/j.dsr2.2008.12.009>
- Telszewski, M., Chazottes, A., Schuster, U., Watson, A. J., Moulin, C., Bakker, D. C. E., et al. (2009). Estimating the monthly pCO₂ distribution in the North Atlantic using a self-organizing neural network. *Biogeosciences*, 6(8), 1405–1421. <https://doi.org/10.5194/bg-6-1405-2009>
- Wanninkhof, R. (2014). Relationship between wind speed and gas exchange over the ocean revisited. *Limnology and Oceanography: Methods*, 12(6), 351–362. <https://doi.org/10.4319/lom.2014.12.351>
- Wanninkhof, R., Asher, W. E., Ho, D. T., Sweeney, C. S., & McGillis, W. R. (2009). Advances in quantifying air-sea gas exchange and environmental forcing. *Annual Review of Marine Science*, 1, 213–244. <https://doi.org/10.1146/annurev.marine.010908.163742>
- Wanninkhof, R., Doney, S. C., Takahashi, T., & McGillis, W. R. (2002). The effect of using time-averaged winds on regional air-sea CO₂ fluxes. In M. Donelan, W. Drennan, E. Saltzman, & R. Wanninkhof (Eds.), *Gas transfer at water surfaces, Geophysical monograph* (Vol. 127, pp. 351–357). AGU.
- Wanninkhof, R., Trinanes, J. A., Pierrot, D., Munro, D. R., Sweeney, C., & Fay, A. R. (2024). AOML_ET: Partial pressure of CO₂ (pCO₂) and sea-air CO₂ fluxes for the global ocean, along with the predictor variables from 1998-01-01 to 2023-12-30, using an Extra Trees (extremely randomized trees) machine learning (NCEI Accession 0298989) [Dataset]. *NCEI*. <https://doi.org/10.25921/0s8y-q287>
- Wanninkhof, R., Park, G.-H., Chelton, D., & Resien, C. (2011). Impact of small-scale variability on air-sea CO₂ fluxes. In S. Komori, W. McGillis, & R. Kurose (Eds.), *Gas transfer at water surfaces 2010* (pp. 431–444). Kyoto University Press.

- Wanninkhof, R., Pickers, P. A., Omar, A. M., Sutton, A., Murata, A., Olsen, A., et al. (2019). A surface ocean CO₂ reference network, SOCONET and associated marine boundary layer CO₂ measurements. *Frontiers in Marine Science*, 6, 400. <https://doi.org/10.3389/fmars.2019.00400>
- Wanninkhof, R., Pierrot, D., Sullivan, K., Mears, P., & Barbero, L. (2022). Comparison of discrete and underway CO₂ measurements: Inferences on the temperature dependence of the fugacity of CO₂ in seawater. *Marine Chemistry*, 247, 104178. <https://doi.org/10.1016/j.marchem.2022.104178>
- Watson, A. J., Schuster, U., Shutler, J. D., Holding, T., Ashton, I. G. C., Landschützer, P., et al. (2020). Revised estimates of ocean-atmosphere CO₂ flux are consistent with ocean carbon inventory. *Nature Communications*, 11(1), 4422. <https://doi.org/10.1038/s41467-020-18203-3>
- Woolf, D. K., Shutler, J. D., Goddijn-Murphy, L., Watson, A. J., Chapron, B., Nightingale, P. D., et al. (2019). Key uncertainties in the recent air-sea flux of CO₂. *Global Biogeochemical Cycles*, 33(12), 1548–1563. <https://doi.org/10.1029/2018GB006041>
- Wu, Z., Wang, H., Liao, E., Hu, C., Edwing, K., Yan, X.-H., & Cai, W.-J. (2024). Air-sea CO₂ flux in the Gulf of Mexico from observations and multiple machine-learning data products. *Progress in Oceanography*, 223, 103244. <https://doi.org/10.1016/j.pocean.2024.103244>
- Yang, M., Bell, T. G., Bidlot, J.-R., Blomquist, B. W., Butterworth, B. J., Dong, Y., et al. (2022). Global synthesis of air-sea CO₂ transfer velocity estimates from ship-based eddy covariance Measurements. *Frontiers in Marine Science*, 9. <https://doi.org/10.3389/fmars.2022.826421>
- Zeng, J., Nojiri, Y., Landschützer, P., Telszewski, M., & Nakaoka, S. (2014). A global surface ocean fCO₂ climatology based on a feed-forward neural network. *Journal of Atmospheric and Oceanic Technology*, 31(8), 1838–1849. <https://doi.org/10.1175/JTECH-D-13-00137.1>